# Observation of an intermediate to $H_2$ binding in a metal–organic framework

Brandon R. Barnett[1,2], Hayden A. Evans[3], Gregory M. Su[4], Henry Z. H. Jiang[1,2], Romit Chakraborty[1,2], Didier Banyeretse[5], Tyler J. Hartman[5], Madison B. Martinez[6], Benjamin A. Trump[3], Jacob D. Tarver[3], Matthew N. Dods[7], Lena M. Funke[1,7], Jonas Börgel[1], Jeffrey A. Reimer[2,7], Walter S. Drisdell[4], Katherine E. Hurst[6], Thomas Gennett[6,8], Stephen A. FitzGerald[5], Craig M. Brown[3,9], Martin Head-Gordon[1,4], and Jeffrey R. Long[1,2,7*]

[1]Department of Chemistry, University of California, Berkeley, Berkeley, California 94720, United States

[2]Materials Sciences Division, Lawrence Berkeley National Laboratory, Berkeley, California, 94720, United States

[3]Center for Neutron Research, National Institute of Standards and Technology, Gaithersburg, Maryland 20899, United States

[4]Chemical Sciences Division, Lawrence Berkeley National Laboratory, Berkeley, California 94720, United States

[5]Department of Physics, Oberlin College, Oberlin, Ohio 44074, United States

[6]Chemistry & Nanoscience Center, National Renewable Energy Laboratory, Golden, Colorado 80401, United States

[7]Department of Chemical and Biomolecular Engineering, University of California, Berkeley, Berkeley, California 94720, United States

[8]Department of Chemistry, Colorado School of Mines, Golden, Colorado 80401, United States

[9]Chemical and Biomolecular Engineering, University of Delaware, Newark, Delaware 19716, United States

*Correspondence to: jrlong@berkeley.edu (J. R. L.)

**Coordinatively-unsaturated metal sites within certain zeolites and metal–organic frameworks can strongly adsorb various molecules[1-4]. While many classical examples involve electron-poor metal cations that interact with adsorbates largely through electrostatic interactions, unsaturated electron-rich metal centers housed within porous frameworks can often chemisorb guests amenable to redox activity or covalent bond formation.[5-9] Despite the promise that materials bearing such sites hold in addressing myriad challenges in gas separations and storage[10-12], very few studies have directly interrogated mechanisms of chemisorption at open metal sites within porous frameworks. Here, we show that non-dissociative chemisorption of $H_2$ at the trigonal pyramidal $Cu^+$ sites in the metal–organic framework $Cu^I$-MFU-4*l*[13] occurs via the intermediacy of a metastable physisorbed precursor species. *In situ* powder neutron diffraction experiments enable crystallographic characterization of this intermediate, the first time that this has been accomplished for any material. Support for a precursor intermediate is also afforded from temperature-programmed desorption and density functional theory calculations. The activation barrier separating the precursor species from the chemisorbed state is shown to correlate with a change in the $Cu^+$ coordination environment that enhances π-backbonding with $H_2$. Ultimately, these findings demonstrate that adsorption at framework metal sites does not always follow a concerted pathway and underscore the importance of probing kinetics in the design of next-generation adsorbents.**

The chemisorption of small diatomic molecules such as $H_2$, $N_2$, $O_2$, CO, and NO on metal surfaces has been thoroughly studied, owing its relevance to important catalytic cycles[14-15]. Many chemisorption events require that a detectable activation barrier be overcome, a process known as "activated chemisorption." Both activated and non-activated chemisorption can involve the intermediacy of physisorbed precursor species, which represent local minima on the potential energy surface[14-17]. Evidence for precursor-mediated adsorption often relies on advanced spectroscopic or molecular beam experiments[18-19], and the validity of adsorption pathways involving precursors has at times spurred considerable debate[20-21].

Certain zeolites and metal–organic frameworks feature coordinatively-unsaturated metal cations that can act as strong adsorption sites for various guest species, although the typically electron-poor nature of these sites tends to favor physical, rather than chemical, adsorption processes[1-4]. There has, however, been a growing interest in the synthesis of porous materials bearing electron-rich metal sites primed to engage in covalent interactions with small molecule adsorbates[5-9]. While such adsorbents may engender more exothermic adsorption and therefore higher uptake capacities, chemisorption can also give rise to transport-independent activation barriers akin to those often observed on surfaces[14-15]. Understanding the kinetic profile for chemisorptive events within porous media is critical toward the design and engineering of adsorptive storage and separation processes[12,22], and the presence of even modest activation barriers may become problematic for applications that require loading or operation at low temperatures.

To address the lack of studies examining chemisorption kinetics at open metal sites in porous solids, we have investigated the mechanism of $H_2$ adsorption at the trigonal pyramidal $Cu^+$ sites within the metal–organic framework $Cu_xZn_{5-x}Cl_{4-x}(btdd)_3$ ($Cu^I$-MFU-4*l*; $H_2$btdd = bis(1*H*-1,2,3-triazolo[4,5-*b*],[4',5'-*i*])dibenzo[1,4]dioxin), which have previously been shown to engage in π-backbonding with $H_2$ and other π-acidic adsorbates[13]. Herein, we demonstrate that non-dissociative chemisorption of $H_2$ at these sites occurs through a physisorbed precursor

intermediate, which is observable via powder neutron diffraction, representing the first crystallographic characterization of a precursor species in a chemisorption process. Temperature-programmed desorption and adsorption kinetics measurements are used to confirm the presence of this species and estimate the chemisorption activation barrier, respectively. Computational analysis further reveals that activation of $H_2$ is associated with a local distortion of the $Cu^+$ coordination environment that augments its π-backbonding capability. Together, these results holistically demonstrate precursor-mediated adsorption in a porous material.

## *In situ* Powder Neutron Diffraction Measurements

The cubic metal–organic framework $Zn_5Cl_4(btdd)_3$ (MFU-4*l*) is comprised of pentanuclear zinc nodes bridged by bis-triazolate $btdd^{2-}$ ligands[23]. Approximately half of its $[ZnCl]^+$ units can undergo post-synthetic cation exchange to install three-coordinate $Cu^+$ centers[13] that evoke the trigonal coordination geometries often adopted within cuprous zeolites[24,25]. Previous work determined that this material exhibits an isosteric heat of $H_2$ adsorption of −32 kJ/mol, which is the most exothermic value known for molecular $H_2$ binding in any metal–organic framework to date[13]. We determined the crystal structure of the evacuated $Cu^I$-MFU-4*l* framework at 7 K using powder neutron diffraction (Fig. 1a-b and Supplementary Fig. 1), and the relative occupancies of the exchangeable metal sites were assigned as 55% Cu and 45 % Zn based on the Cu:Zn ratio determined by inductively coupled plasma optical emission spectroscopy (ICP-OES) analysis. In all crystallographic refinements, the tetrahedral $Zn^{2+}$ centers were found to be capped solely with a chloro ligand, which yields an overall chemical formula of $Cu_{2.2}Zn_{2.8}Cl_{1.8}(btdd)_3$[26]. This assignment is supported by $^{13}C\{^1H\}$ solid-state cross polarization NMR and FT-IR spectroscopies, which demonstrate that any formate in the material is present in only very small relative quantities (Supplementary Fig. 2-3). The Fourier difference map (Supplementary Fig. 4) clearly shows the absence of residual density in the vicinity of the Zn–Cl moieties, demonstrating that no ligated formate is present at these sites.

Powder samples of $Cu^I$-MFU-4*l* were dosed with 0.75 $D_2$ molecules per Cu at 40 K and then cooled to 7 K for neutron diffraction data collection (Supplementary Fig. 5). In the resulting structure, $D_2$ was located ~1.6 Å from the unsaturated $Cu^+$ centers (site I, Fig. 1c), indicating very strong binding. This value is also consistent with the Cu–$H_2$ distance of 1.7 Å calculated previously for the material using density functional theory (DFT)[27], but the occupancy of the site is only 0.087(18) $D_2$ molecules per Cu and thus represents a small fraction of the total adsorbed hydrogen (Table 1). The highest occupancy site (site II) is located at the windows of the pentanuclear tetrahedral nodes. Site II is characterized by weak physisorption and likely serves as the primary adsorption site in the parent MFU-4*l* material, for which the isosteric heat of $H_2$ adsorption was measured to be −5 kJ/mol at low coverage[23]. One additional site (site I*) is also occupied under these conditions, located directly above site I and ~3 Å away from the strongly adsorbing $Cu^+$ centers. Importantly, despite the difficulties posed by compositional disorder of $Cu^+$ and $[Zn–Cl]^+$ in this system, refinements strongly suggest that density is present at this position only following $D_2$ dosing. However, the compositional disorder conspires with powder averaging to obfuscate the occupancy of $D_2$ at site I*. Indeed, the occupancy of this site was found to be particularly sensitive to the thermal parameters employed, consistent with a significant degree of $D_2$ disorder or dynamics. Owing to additional compositional disorder at the

metal sites, we modeled the thermal parameters of $D_2$ at site I* conservatively, so as to not overestimate its contribution to the total amount of adsorbed $D_2$ (Supplementary Table 1).

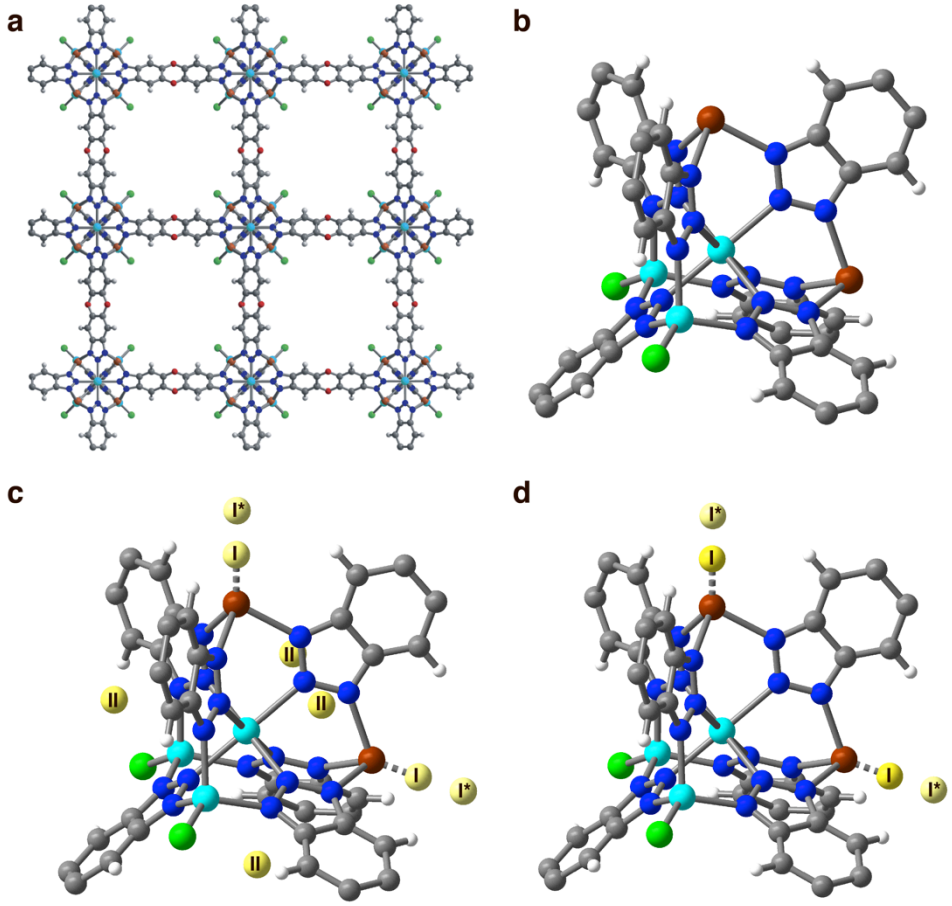


**Fig. 1 Crystal structures of evacuated and $D_2$-dosed $Cu^I$-MFU-4*l*.** **a**, A portion of the structure of activated $Cu^I$-MFU-4*l*, as determined from powder neutron diffraction data. **b**, Expanded view of the pentanuclear nodes comprising the secondary building units of the framework. **c**, Structure of $Cu^I$-MFU-4*l* obtained at 7 K after dosing with 0.75 $D_2$ molecules per Cu at 40 K and cooling to 7 K. **d**, Structure obtained at 7 K following dosing with 0.75 $D_2$ molecules per Cu at 77 or 300 K. Cyan, brown, green, blue, grey, and white spheres represent Zn, Cu, Cl, N, C, and H atoms, respectively; yellow spheres represent isotropically refined $D_2$ molecules.

The separation between sites I and I* is approximately 30% of the nearest neighbor $D_2\cdots D_2$ separation in solid $D_2$[28], and thus it is clear that both sites cannot be occupied simultaneously at a single $Cu^+$ center. Instead, this proximity suggests an activation barrier to $D_2$ binding at site I, with site I* representing a metastable physisorbed state that serves as a precursor to chemisorption. To further investigate this idea, a sample of activated $Cu^I$-MFU-4*l* was dosed with 0.75 $D_2$ molecules per Cu at successively higher temperatures (Supplementary Fig. 6-7). Following dosing at 77 K and subsequent cooling to 7 K, $D_2$ was found to occupy sites I and I* exclusively (Fig. 1 and table S1). Importantly, the occupancy of site I is much larger here than

when dosed at 40 K, yet it remains significantly lower than 0.75 $D_2$ molecules per Cu. Increasing the dosing temperature to 300 K yields a further increase in the occupancy of site I. The increasing occupancy of site I with dosing temperature is strongly correlated with an isotropic framework contraction as shown by the decreasing value of cubic lattice parameter *a* (Table 1).

**Table 1. Occupancies of $D_2$ at site I and cubic lattice parameter *a*, determined from powder neutron diffraction data obtained after dosing the evacuated framework with 0.75 equivalents of $D_2$ per Cu at the specified temperature.[a]**

| Dosing Temperature (K) | Site I Occupancy | *a* (Å) |
|---|---|---|
| **40** | 0.087(18) | 31.2174(10) |
| **77** | 0.350(18) | 31.1652(10) |
| **300** | 0.513(14) | 31.1505(6) |

[a]All diffraction data were collected at 7 K, and the super-atom approach was used to model $D_2$ molecules as isotropic D atoms[29-31]. Occupancies are expressed as molecular equivalents of $D_2$ per Cu. The value of *a* for the evacuated framework at 7 K is 31.2744(14) Å.

Binding of $H_2$ at site I* can be described as a physisorbed precursor state, representing a local minimum on the potential energy surface of adsorption[16,17,19,21]. While surface science often relies on spectroscopic or molecular beam experiments to provide indirect evidence for precursor-mediated adsorption[18,19], the spatial separation of $Cu^+$ centers in $Cu^I$-MFU-4*l* allows for the trapping and direct observation of this metastable precursor state at low temperatures. Accordingly, the kinetic nature of hydrogen adsorption at the $Cu^+$ sites in $Cu^I$-MFU-4*l* is more reminiscent of chemisorption on metallic surfaces than of the classical, barrierless physisorption generally observed within porous solids. To our knowledge, this is the first demonstration of a precursor-mediated adsorption within a porous solid.

## Temperature-Programmed Desorption and Kinetics Measurements

Given the compositional disorder inherent to $Cu^I$-MFU-4*l*, we sought to experimentally probe $H_2$ sorption at $Cu^+$ in a site-specific manner. Temperature-programmed desorption (TPD) was identified as a promising technique, given the much higher temperature required for $H_2$ desorption from $Cu^+$ compared to other sites in the framework[27]. Accordingly, a powder sample of $Cu^I$-MFU-4*l* was first dosed with a known molar quantity of $H_2$ (substoichiometric with respect to $Cu^+$). For samples dosed at 293 K, the sample cell was subsequently cooled to a base temperature of 20 K prior to heating and data collection. A single high-temperature desorption feature ($T_{max}$ = 244 K) is present following $H_2$ loading at 293 K (Fig. 2 and Supplementary Fig. 10-12)[27]. In contrast, for samples that are cold-loaded with $H_2$ at 20 K, a new desorption peak becomes evident at a moderately lower temperature ($T_{max}$ = 216 K). This temperature is far too high to arise from desorption of $H_2$ that is not bound to a metal site (*e.g.* from crystallographic site II), as any hydrogen at such sites desorbs below 100 K (see Supplementary Fig. 10 and Ref. 27), but is very much consistent with desorption of $H_2$ from the crystallographically located precursor site at $Cu^+$ (I*). In agreement with the neutron diffraction results, TPD indicates that low-temperature dosing inhibits chemisorption and allows for trapping of some $H_2$ at the precursor site. However, desorption from the precursor site requires temperatures that are

sufficiently high to overcome the chemisorption activation barrier, and accordingly some chemisorption does take place during the heating phase of the TPD experiment. These competing phenomena result in desorption peaks for both sites at $Cu^+$ being present for cold-loaded samples.

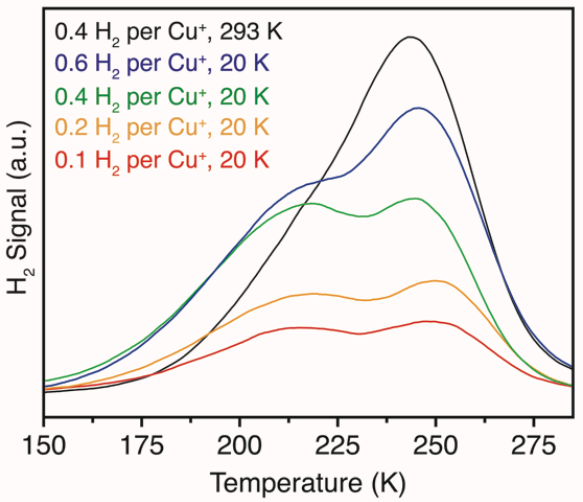


**Fig. 2 Temperature-programmed $H_2$ desorption data.** Thermal desorption data obtained for $Cu^I$-MFU-4*l* after loading with $H_2$ at 293 or 20 K. The desorption data obtained following loading at 20 K feature a second, lower-temperature peak that can be assigned to desorption of $H_2$ directly from the physisorbed precursor state.

Hydrogen adsorption kinetics measurements were performed between 276-300 K. The transient adsorption data were fit to a Langmuir first-order rate law[32], which yielded an activation energy $E_a$ = 9.0 kJ/mol (Supplementary Fig. 13-15). This treatment omits the contribution that changing the temperature will have on the barrierless physisorption equilibrium at the precursor site[33], and accordingly is best interpreted as a lower bound for the actual chemisorption activation barrier. Importantly, our measured lower bound value for $E_a$ is an order of magnitude larger than the barrier to $H_2$ diffusion anticipated within this large-pore framework material[34], strongly indicating that our kinetics data are reflective of a transport-independent activation barrier. The measured $E_a$ is also too large to arise from a pathway involving $H_2$ desorption from site II and subsequent non-activated chemisorption at site I, for which the activation barrier would be equal in magnitude to the enthalpy of adsorption at site II (–5 kJ/mol)[14]. Accordingly, both TPD and adsorption kinetics further substantiate the role of a precursor intermediate to hydrogen chemisorption at $Cu^+$, and provide support for the legitimacy of adsorption site I* in the structural model constructed from neutron diffraction data.

**Density Functional Theory Calculations**

In order to assess further the structural and electronic changes that occur upon non-dissociative chemisorption of $H_2$ at $Cu^+$, we performed DFT calculations on a pentanuclear cluster model that represents a single framework node (Supplementary Fig. 16-18). Binding of hydrogen to $Cu^+$

was found to be associated with a decrease in the average framework Zn($O_h$)–N distance, which can reasonably be assumed as the cause of the isotropic framework contraction, given that the octahedral $Zn^{2+}$ site represents the geometric center of the framework building unit. In addition, the calculations indicate that $H_2$ binding results in $Cu^+$ moving away from the octahedral $Zn^{2+}$ site by ~0.25 Å (Fig. 3a and Supplementary Fig. 19), resulting in an increased pyramidalization of the $Cu^+$ coordination sphere. This change in turn destabilizes the degenerate $d_\pi$ orbitals (*e* in $C_{3v}$ symmetry) that are of proper symmetry to form the π component of the Cu–$H_2$ interaction (Fig. 3b). Accordingly, $Cu^+$ migration appears to facilitate enhanced π-backdonation to $H_2$. Support for this argument is found via an energy decomposition analysis[35] of the absolutely localized molecular orbitals corresponding to the Cu–$H_2$ bonding interaction (Supplementary Table 2). For a cluster with all coordinates fully relaxed, Cu→$H_2$ backdonation contributes −24.4 kJ/mol to the total interaction energy, which is larger than the $H_2$→Cu forward donation contribution of −21.7 kJ/mol. However, for a cluster wherein only the $H_2$ coordinates are allowed to relax while binding to the bare cluster (*i.e.* no migration of $Cu^+$ occurs), this analysis predicts much weaker backdonation (−11.9 kJ/mol), while forward donation decreases more modestly to −15.8 kJ/mol. Accordingly, these results illuminate an intricate relationship between local structural effects contributing to Cu–$H_2$ π-backbonding and the contraction of the larger three-dimensional framework.

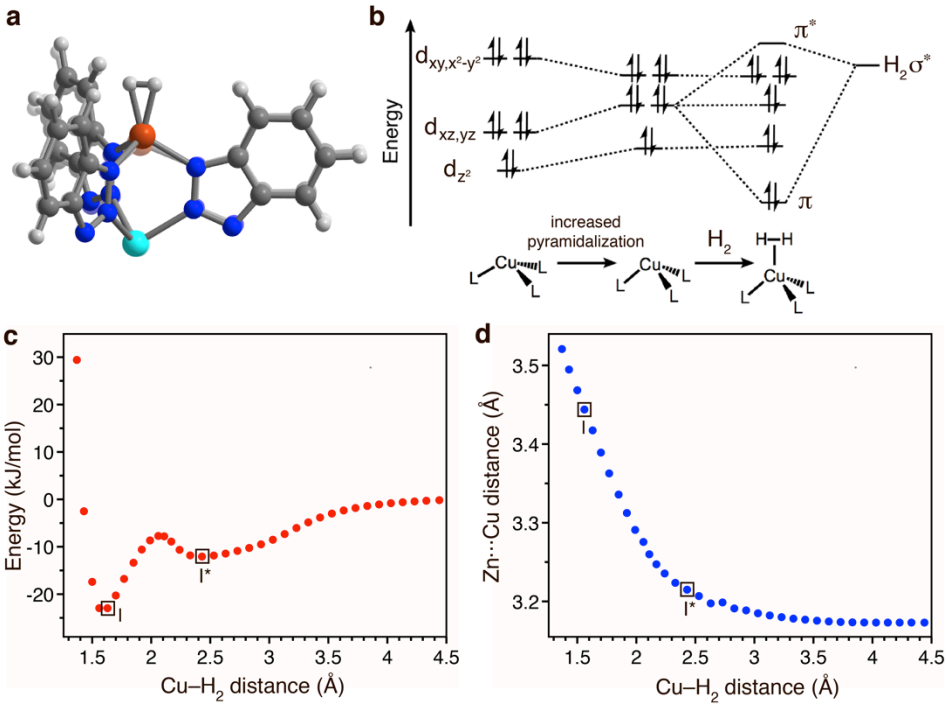


**Fig. 3 Structural and electronic changes associated with $H_2$ binding in $Cu^I$-MFU-4*l*. a**, A portion of the DFT-optimized cluster model, with (solid structure) and without (faded structure) $H_2$ bound to $Cu^+$. **b**, Qualitative molecular orbital energy diagram illustrating how the Cu 3d orbitals are affected by pyramidalization and π-backbonding to $H_2$. Interactions between $Cu^+$ and $H_2$ of σ symmetry are omitted for clarity. **c**, Calculated potential energy surface along the Cu–$H_2$ coordinate at the B3LYP-D2/6-31++G**(6-31G*) level of DFT. **d**, Calculated relationship between the Zn···Cu distance and Cu–$H_2$ distance at the B3LYP-D2/6-31++G**(6-31G*) level of DFT.

A scan of the potential energy surface (PES) along the Cu–$H_2$ coordinate revealed a local minimum corresponding to a physisorbed precursor (Fig. 3c), albeit under rather specific basis set conditions. At the B3LYP-D2/6-31++G**(6-31G*) level of theory, the optimized structure of the species corresponding to this local minimum shows $H_2$ bound end-on (Supplementary Fig. 16) with a Cu–$H_2$(centroid) distance of 2.43 Å (Fig. 3c). Importantly, the central Zn···Cu distance in this structure is nearly unchanged from that without $H_2$ present. As shown in Fig. 3d, $Cu^+$ migration occurs at increasingly shorter Cu–$H_2$ distances, with the potential energy saddle point occurring at Zn···Cu distance of 2.28 Å, corresponding to a Cu–$H_2$ separation of 2.06 Å. The calculated barrier separating the shallow well of this local minimum structure from that of the chemisorbed species is 4.4 kJ/mol, which is smaller than the lower bound of 12.7 kJ/mol measured experimentally via adsorption kinetics. Analogous scans of the PES using the def2-TZVPPD(def2-SVP) basis set yield only a shoulder, rather than a true minimum, at Cu–$H_2$(centroid) distances between 2 and 3 Å (Supplementary Fig. 21). The difficulties in quantitatively modeling the kinetic pathway of $H_2$ chemisorption can likely be traced to the increased flexibility available to a single cluster node relative to the extended lattice. Unfortunately, calculation of the PES using a larger computational model that mimics the extended lattice would not be tractable with the modern range separated hybrid functionals employed here. Nevertheless, it is notable that qualitative evidence for precursor-mediated chemisorption can be garnered through analysis of a single cluster node, and these data suggest that the experimental kinetic pathway arises from both local and long-range structural effects.

**Spectroscopic evidence for π-backbonding upon $H_2$ binding**

X-ray absorption spectroscopy (XAS) data were collected at the Cu L-edge for evacuated and $H_2$-dosed samples of $Cu^I$-MFU-4*l* to investigate experimentally the electronic character of the $Cu^+$–$H_2$ interaction upon non-dissociative chemisorption. Importantly, XAS serves as an excellent probe of electronic perturbations of the valence d manifold[36]. The spectrum for activated $Cu^I$-MFU-4*l* displays $L_3$ and $L_2$ edge features at 936 and 956 eV, respectively (Fig. 4a)[37]. Given the absence of a pure 3d hole for electron excitation, these transitions arise due to mixing of Cu 3d character into vacant orbitals of largely σ* character[38]. Following *in situ* $H_2$ dosing at 25 ºC, the $L_3$ and $L_2$ edge features shift to lower energies by approximately 0.5 and 0.7 eV, respectively, and grow in intensity with increasing $H_2$ pressure from 200 to 1000 mbar. Based on complementary $H_2$ adsorption isotherm data (Supplementary Fig. 22), only partial coverage of the $Cu^+$ sites with $H_2$ is achieved under these conditions, and thus the edges consist of superimposed peaks from coordinatively-unsaturated and $H_2$-bound $Cu^+$ centers. Nevertheless, the increase in edge intensity with $H_2$ dosing can be directly traced to increased metal-to-ligand charge transfer via π-backdonation[36,37,39].

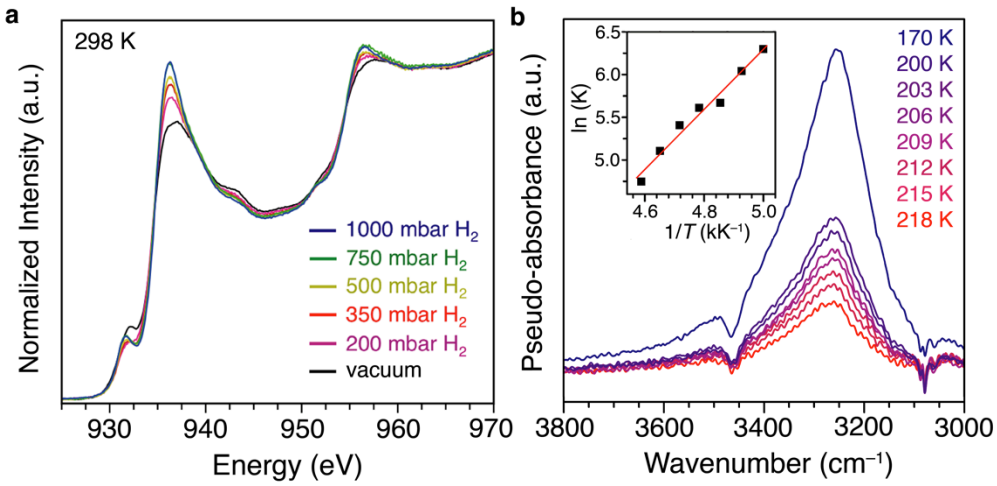


**Fig. 4 Spectroscopic evidence of π-backbonding. a**, *In situ* Cu L-edge X-ray absorption spectra for evacuated $Cu^{I}$-MFU-4*l* (black) and after dosing with various pressures of $H_2$ at 25 °C. **b**, Fundamental *ν*(H–H) vibration at a constant $H_2$ loading at different temperatures, with the inset showing the corresponding van't Hoff plot and linear regression used to determine $\Delta H°_{ads}$ and $\Delta S°_{ads}$.

For physisorbed $H_2$, the vibrational energy of the fundamental *ν*(H–H) band is generally modestly red-shifted relative to that of the free molecule (4050–4150 versus 4161 $cm^{-1}$)[40,41]. In contrast, the *in situ* DRIFTS spectrum of $Cu^{I}$-MFU-4*l* dosed with $H_2$ exhibits a broad feature of weak intensity centered at 3252 $cm^{-1}$, corresponding to the fundamental *ν*(H–H) stretch (Fig. 4b)[42]. Using the spectrum for the $D_2$-dosed material as a baseline, we were able to isolate this band from framework vibrations and obtain a difference spectrum with peaks associated only with chemisorbed $H_2$ or $D_2$ (Supplementary Fig. 23). Unlike most molecular Kubas complexes[43], $Cu^{I}$-MFU-4*l* offers a unique opportunity to study the thermodynamics of $H_2$ binding to a low-valent metal site directly and without consideration of a prior ligand dissociation step. To this end, variable-temperature DRIFTS data were collected for a sample of the $H_2$-dosed framework between 200 and 218 K (Fig. 4b). Integration of the corresponding *ν*(H–H) peak enabled calculation of the fractional coverage by comparison to the peak area under saturation conditions (170 K)[44,45]. A van't Hoff analysis afforded an enthalpy value $\Delta H°_{ads}$ = −28(2) kJ/mol and entropy value $\Delta S°_{ads}$ = −89(8) J/(mol·K)). These values are in good agreement with the thermodynamic parameters calculated from DFT (Supplementary Table 3) and with the isosteric heat of adsorption measured previously from gas adsorption data[13].

## Outlook

The soft, electron-rich $Cu^{+}$ sites present in $Cu^{I}$-MFU-4*l* serve as a counterpoint to the hard, Lewis acidic open metal sites accessible in many metal–organic frameworks and zeolites, and their aptitude for π-backbonding leads to non-dissociative hydrogen binding via chemisorption. The resulting large magnitude of $\Delta H°_{ads}$ renders this framework an intriguing candidate for adsorptive hydrogen storage at ambient and even elevated temperatures[12]. However, this study clearly illustrates the kinetic complexities that can be associated with chemisorption in porous materials, and reinforces the importance of analyzing adsorption kinetics in chemisorption-driven processes. We anticipate that physisorbed precursors will be realized as relevant

intermediates in other chemisorption processes within porous solids, and hope this work provides a roadmap for designing experiments that will enable their identification.

**References and Notes:**


1. Kulprathipanja, S., Ed. *Zeolites in industrial separation and catalysis*. 1st Ed. (Wiley-VCH Verlag GmbH & Co. KGaA, Weinheim, 2010).

2. Li, J.-R., Kuppler, R. J. & Zhou, H.-C. *Chem. Soc. Rev.* **38**, 1477–1504 (2009).

3. Dincă, M. & Long, J. R. Hydrogen storage in microporous metal–organic frameworks with exposed metal sites. *Angew. Chem. Int. Ed.* **47**, 6766–6779 (2008).

4. Yaghi, O. M., Kalmutzki, M. J. & Diercks, C. S. *Introduction to reticular chemistry: Metal–organic frameworks and covalent organic frameworks* (Wiley-VCH Verlag & Co. KGaA, Weinheim, 2019).

5. Bloch, E. D. *et al.* Selective binding of $O_2$ over $N_2$ in a redox-active metal–organic framework with open iron(II) coordination sites. *J. Am. Chem. Soc.* **133**, 14814–14822 (2011).

6. Anderson, J. S., Gallagher, A. T., Mason, J. A. & Harris, T. D. *J. Am. Chem. Soc.* **136**, 16489–16492 (2014).

7. Reed, D. A. *et al.* A spin transition mechanism for cooperative adsorption in metal–organic frameworks. *Nature* **274**, 96–100 (2017).

8. Zhang, J.-P. & Kitagawa, S. Supramolecular isomerism, framework flexibility, unsaturated metal center, and porous property of Ag(I)/Cu(I) 3,3',5,5'-tetramethyl-4,4'bipyrazolate. *J. Am. Chem. Soc.* **130**, 907–917 (2008).

9. Burgun, A. *et al.* Mapping-out catalytic processes in a metal–organic framework with single-crystal X-ray crystallography. *Angew. Chem. Int. Ed.* **56**, 8412–8416 (2017).

10. Sato, H. *et al.* Self-accelerating CO sorption in a soft nanoporous crystal. *Science* **343**, 167–170 (2014).

11. Lee, K. *et al.* Design of a metal–organic framework with enhanced back bonding for separation of $N_2$ and $CH_4$. *J. Am. Chem. Soc.* **136**, 698–704 (2014).

12. Allendorf, M. D. *et al.* An assessment of strategies for the development of solid-state adsorbents for vehicular hydrogen storage. *Energy Environ. Sci.* **11**, 2784–2812 (2018).

13. Denysenko, D., Grzywa, M., Jelic, J., Reuter, K. & Volkmer, D. Scorpionate-type coordination in MFU-4*l* metal–organic frameworks: Small-molecule binding and activation upon the thermally activated formation of open metal sites. *Angew. Chem. Int.*

*Ed*. **53**, 5832–5836 (2014).

14. Masel, R. I. *Principles of adsorption and reaction on solid surfaces* (John Wiley & Sons, Inc., New York, NY, 1996).

15. Kolasinski, K. W. *Surface science: Foundations of catalysis and nanoscience* (John Wiley & Sons, Inc., Hoboken, NJ, Ed. 2, 2008).

16. Bowker, M. The role of precursor states in adsorption, surface reactions and catalysis. *Top. Catal*. **59**, 663–670 (2016).

17. Brown, D. E., Moffatt, D. J. & Wolkow, R. A. Isolation of an intrinsic precursor to molecular chemisorption. *Science* **279**, 542–544 (1998).

18. Rendulic, K. D. & Winkler, A. Adsorption and desorption dynamics as seen through molecular beam techniques. *Surface Sci*. **299–300**, 261–276 (1994).

19. Beutl, M., Rendulic, K. D. & Castro, G. R. Does the rotational state of a molecule influence trapping in a precursor? An investigation of $N_2$/W(100), CO/FeSi(100) and $O_2$/Ni(111). *Surface Sci*. **385**, 97–106 (1997).

20. Grunze, M. & Kreuzer, H. J., Eds., *Kinetics of interface reactions* (Springer-Verlag, Berlin, 1986), Vol. 8.

21. Beutl, M. *et al.* There is a true precursor for hydrogen adsorption after all: the system $H_2$/Pd(111) + subsurface V. *Chem. Phys. Lett*. **342**, 473–478 (2001).

22. Martell, J. D., Milner, P. J., Siegelman, R. L. & Long, J. R. Kinetics of cooperative $CO_2$ adsorption in diamine-appended variants of the metal–organic framework $Mg_2$(dobpdc). *Chem. Sci.* **11**, 6457–6471.

23. Denysenko D. *et al.*, Elucidating gating effects for hydrogen sorption in MFU-4-type triazolate-based metal-organic frameworks featuring different pore sizes. *Chem. Eur. J.* **17**, 1837–1848 (2011).

24. Fowkes, A. J., Ibberson, R. M. & Rosseinsky, M. J. Structural characterization of the redox behavior in copper-exchanged sodium zeolite Y by high-resolution powder neutron diffraction. *Chem. Mater.* **14**, 590–602 (2002).

25. Ipek, B., Pollock, R. A., Brown, C. M., Uner, D. & Lobo, R. F. $H_2$ adsorption on Cu(I)-SSZ-13. *J. Phys. Chem. C* **122**, 540–548 (2018).

26. For more on our choice of crystallographic model, see the Supplementary Information.

27. Weinrauch, I. *et al.*, Capture of heavy hydrogen isotopes in a metal-organic framework with active Cu(I) sites. *Nat. Commun*. **8**, 14496 (2017).

28. Van Kranendonk, J. & Gush, H. P. The crystal structure of solid hydrogen. *Phys. Lett*. **1**, 22–23 (1962).

29. Pollock, R. A., Her, J.-H., Brown, C. M., Liu, Y. & Dailly, A. Kinetic trapping of $D_2$ in MIL-53(Al) observed using neutron scattering. *J. Phys. Chem. C* **118**, 18197–18206 (2014).

30. Wu, H., Zhou, W. & Yildirim, T. Hydrogen storage in a prototypical zeolitic imidazolate framework-8. *J. Am. Chem. Soc.* **129**, 5314–5315 (2007).

31. Brown, C. M., Liu, Y., Yildirim, T., Peterson, V. K. & Kepert, C. J. Hydrogen adsorption in HKUST-1: a combined inelastic neutron scattering and first-principles study. *Nanotechnology* **20**, 204025 (2009).

32. Liu, Y. & Shen, L. From Langmuir kinetics to first- and second-order rate equations for adsorption. *Langmuir* **24**, 11625–11630 (2008).

33. Wei, J. Nonlinear phenomena in zeolite diffusion and reaction. *Ind. Eng. Chem. Res.* **33**, 2467–2472 (1994).

34. Saha, D., Wei, Z. & Deng, S. Hydrogen adsorption equilibrium and kinetics in metal–organic framework (MOF-5) synthesized with DEF approach. *Sep. Purif. Technol.* **64**, 280–287 (2009).

35. Khaliullin, R. Z., Cobar, E. A., Lochan, R. C., Bell, A. T. & Head-Gordon, M. Unraveling the origin of intermolecular interactions using absolutely localized molecular orbitals. *J. Phys. Chem. A* **111**, 8753–8765 (2007).

36. Hocking, R. K. *et al.* Fe L-Edge XAS studies of $K_4[Fe(CN)_6]$ and $K_3[Fe(CN)_6]$: A direct probe of back-bonding. *J. Am. Chem. Soc.* **128**, 10442–10451 (2006).

37. Su, G. M. *et al.* Backbonding contributions to small molecule chemisorption in a metal–organic framework with open copper(I) centers. *Chem. Sci*. **12**, 2156–2164 (2021).

38. Harkins, S. B., Mankad, N. P., Miller, A. J. M., Szilagyi, R. K. & Peters, J. C. Probing the electronic structures of $[Cu_2(\mu\text{-}XR_2)]^{n+}$ diamond cores as a function of the bridging X atom (X = N or P) and charge (n = 0, 1, 2). *J. Am. Chem. Soc*. **130**, 3478–3485 (2008).

39. George, S. J., Lowery, M. D., Solomon, E. I., Cramer, S. P. Copper L-edge spectral studies: A direct experimental probe of the ground-state covalency in the blue copper site in plastocyanin. *J. Am. Chem. Soc.* **115**, 2968–2969 (1993).

40. Vitillo, J. G. *et al.* Role of exposed metal sites in hydrogen storage in MOFs. *J. Am. Chem. Soc*. **130**, 8386–8396 (2008).

41. M. T. Kapelewski *et al.*, $M_2$(*m*-dobdc) (M = Mg, Mn, Fe, Co, Ni) Metal–organic frameworks exhibiting increased charge density and enhanced $H_2$ binding at the open metal sites. *J. Am. Chem. Soc*. **136**, 12119–12129 (2014).

42. FitzGerald, S. A., Mukasa, D., Rigdon, K. H., Zhang, N. & Barnett, B. R. Hydrogen isotope separation within the metal–organic framework Cu(I)-MFU-4*l*. *J. Phys. Chem. C*. **123**, 30427–30433 (2019).

43. Kubas, G. J. *Metal dihydrogen and σ-bond complexes: Structure, theory and reactivity* (Kluwer Academic/Plenum Publishers, New York, NY, 2001).

44. Garrone, E. & Otero Areán, C. Variable temperature infrared spectroscopy: A convenient tool for studying the thermodynamics of weak solid–gas interactions. *Chem. Soc. Rev.* **34**, 846 (2005).

45. FitzGerald, S. A. *et al.* Metal-specific interactions of $H_2$ adsorbed within isostructural metal–organic frameworks. *J. Am. Chem. Soc*. **133**, 20310–20318 (2011).

## Methods

**General synthesis and characterization methods.** Unless otherwise stated, reagent-grade starting materials were purchased from commercial sources and either used as received or purified by standard procedures[46]. Solvents were sparged with Ar, dried over activated 3 Å molecular sieves, and stored in a glovebox prior to use. The framework MFU-4*l* was prepared as described previously[23]. Elemental analyses were performed in the Microanalytical Laboratory at the University of California, Berkeley. Inductively-coupled plasma–optical emission spectroscopy (ICP-OES) measurements were performed on an Optima 7000 DV instrument that is maintained by the Microanalytical Laboratory. Metal–organic framework samples (1-3 mg) analyzed by ICP-OES were digested in a small amount (< 1 mL) of concentrated nitric acid, and then diluted in Milli-Q ultrapure water to a concentration of 1–10 ppm Zn and Cu.

**Synthesis of $Cu^I$-MFU-4*l*.** The framework $Cu^I$-MFU-4*l* was synthesized using a procedure adapted from the literature[13,42]. In an $N_2$-filled glovebox, a *N,N*-dimethylacetamide (DMA) solution of $CuCl_2$ (0.275 g, 2.05 mmol, 20 equiv., 20 mL) was added to activated MFU-4*l* (0.125 g, 0.100 mmol) in a 20 mL borosilicate vial. The vial was capped, placed in a hotplate well, and heated to 60 °C for 20 h. The mother liquor was subsequently decanted, and the sample was soaked in fresh DMA at 60 °C for 12 h. This process was repeated one additional time. After this second soaking, the DMA was decanted, and the framework was soaked in MeOH at 60 °C. The mother liquor was decanted and replaced with fresh MeOH three times over the course of two days (total of four MeOH washes). The resulting green solid was dried *in vacuo* at 60 °C in the glovebox, during which time it slowly became brown in color. The vial was then sealed and transferred to a wet, $O_2$-free glovebox filled with a Praxair Hydrostar® (5% $H_2$ in $N_2$) gas mixture

(*note*: the $H_2$ atmosphere is not necessary for this synthetic protocol). To the framework was added a MeOH solution of lithium formate hydrate (0.400 g, 5.71 mmol, 20 mL). The mixture was allowed to stand at room temperature for 1 h. The mother liquor was then decanted, and the framework was soaked in fresh MeOH at room temperature. This process was repeated four times over the course of 24 h (total of five MeOH washes). The framework was then dried in the glovebox *in vacuo* at 80 °C, yielding $Cu^{II}$-MFU-4*l*-formate as a light green powder. Autoreduction of the $Cu^{2+}$ centers to yield $Cu^{I}$-MFU-4*l* was accomplished using a Micromeritics ASAP2020 instrument. A sample of $Cu^{II}$-MFU-4*l*-formate in a glass tube capped with a Transeal was heated *in vacuo* at 100 °C for 12 h, and then ramped at 2 °C/min to 180 °C, where it was held for 3 h. Between 120–180 °C, extensive offgassing occurs, and the sample changes in color from light green to beige.

**Elemental analysis.** Over multiple batches, metals analysis using ICP-OES gave Cu:Zn ratios of approximately 0.75, consistent with a formula of $Cu_{2.2}Zn_{2.8}X_n(btdd)_3$ ($X^-$ = chloride, formate). Lithium content was consistently found to be below the instrument detection limit. Combustion analysis on activated samples of $Cu^{I}$-MFU-4*l* yielded the following CHN percent weights: C, 36.77; H, 1.15; N, 21.08 (average of measurements from three separate batches). For a material with the above metals ratio and a chloride ligand on all of the tetrahedral Zn sites, this would yield a formula of $C_{36}H_{12}N_{18}O_6Cu_{2.2}Zn_{2.8}Cl_{1.8}$, with an expected analysis of: C, 36.66; H, 1.02; N, 21.38. If all of the chlorides were replaced with formate, this would yield a formula of $C_{37.8}H_{13.8}N_{18}O_{9.6}Cu_{2.2}Zn_{2.8}$, with an expected analysis of: C, 37.94; H, 1.16; N, 21.07. Given the significant discrepancy between the carbon contents of this latter theoretical value and that measured for our samples (37.94 vs. 36.77, respectively), we proceeded to model the anionic ligands capping the tetrahedral Zn sites as chlorides in our crystallographic model (see below section on powder neutron diffraction).

**Measurement of hydrogen adsorption isotherm data.** UHP-grade (99.999% purity) $H_2$ and He were used for all adsorption measurements. Gas adsorption isotherms in the pressure range of 0–1.0 bar were measured using a volumetric method on a Micromeritics 3Flex gas sorption analyzer. Samples of $Cu^{I}$-MFU-4*l* were prepared in preweighed analysis tubes capped with a Transeal via autoreduction of $Cu^{II}$-MFU-4*l*-formate *in vacuo* at 180 °C (ramp rate = 2 °C/min) until the outgas rate was determined to be less than 2 μbar/min (approximately 3–4 h). The tube was then weighed and subsequently transferred to the analysis port of the instrument. Free space measurements were performed using He at the analysis temperature. A Julabo F32 water circulator was used as the isothermal bath. Oil-free vacuum pumps and oil-free pressure regulators were used for all measurements to prevent contamination of the samples during evacuation or of the feed gases during isotherm measurements.

**Powder neutron diffraction measurements**. Powder neutron diffraction measurements were performed on 0.362 g $Cu^{I}$-MFU-4*l* at the National Institute of Standards and Technology Center for Neutron Research (NCNR). Data was collected at the high-resolution neutron powder diffractometer, BT1, utilizing a Ge(311) monochromator with an in-pile 60' collimator, corresponding to a neutron wavelength of 2.0775 Å. The activated sample was loaded into a vanadium sample can in a He environment glovebox, and sealed with an indium o-ring onto a copper heating block containing a valved outlet for gas loading. After mounting the sample onto a bottom-loaded closed cycle refrigerator (CCR), the sample was cooled to base temperature for

measurement. For $D_2$ gas dosing, the sample was connected to a fixed-volume gas manifold, heated to $T$ = 40, 77, or 300 K, and cooled back to base temperature for measurement of Rietveld quality data collection (~6 to ~8 h per data set), or at the noted temperature for lattice constant determination (~1 h per data set).

Powder neutron diffraction data were analyzed using the GSAS software suite[47,48]. Initial Le Bail refinements were first conducted to determine a background function, lattice parameters, and peak shapes[49]. The peak shape of the bare model was applied to all subsequent refinements for consistency. The position and orientation of the $btdd^{2-}$ ligands were refined using restraints to ensure planarity/bond lengths in line with chemical reasoning. The super-atom approach was used to approximate the $D_2$ molecule as a single D-atom with double occupancy[29-31].

An extended discussion on the refinement procedures and construction of structure solutions can be found in the Supplementary Text.

**Solid-state Nuclear Magnetic Resonance (NMR) spectroscopy.** $^{13}C\{^1H\}$ cross polarization magic-angle spinning (CP MAS) NMR spectra were measured on a sample of $Cu^I$-MFU-4*l* under an inert atmosphere. A sample of fully activated material was loaded into an air-tight Teflon insert for a 4 mm rotor within the argon atmosphere of a glovebox. The closed rotor was transferred to a 11.7 T magnet and spun under continuous $N_2$ flow at 7.5 kHz. The magic angle ($\theta$ = 54.74°) was set prior to the experiment using KBr and the $^{13}C$ chemical shifts were referenced to 38.5 ppm (adamantane, tertiary carbon − higher frequency resonance)[50]. A contact time of 200 μs was used, and $^1H$ decoupling was carried out with the TPPM pulse scheme. To determine signal intensities, the centerband and all accompanying spinning sidebands were integrated and summed up. In addition to peaks arising from the $btdd^{2-}$ carbon atoms and spinning sidebands, a small peak at 170 ppm is visible that is consistent with the formate anion[51]. Owing to the fact that no formate ligands are visible at the peripheral metal sites through powder neutron diffraction, we contend that any formate present in the material is present exclusively as "free" formate within the pores or as part of a small amount of some amorphous phase not observed in our PND refinements. Peak integration yields an upper bound value of 1 formate anion per 8 $btdd^{2-}$ ligands.

**Temperature-programmed desorption measurements.** TPD measurements utilizing sub-stoichiometric $H_2$ dosing were performed at Oberlin College. Within an argon-filled glovebox, activated $Cu^I$-MFU-4*l* powder (10-47 mg) was transferred to a cylindrical copper cell. In some cases, the powder was compacted inside the cell by pressing on it with a $1/8^{th}$ inch diameter stainless steel rod. The compacted pellet sample could be returned to a loose powder form using a fine-tipped dental tool. All sample manipulations were performed inside the glovebox before sealing the cell using Swagelok fittings to an ORS2 bonnet valve. The sealed cell was removed from the glovebox and mounted to the base of a modified Janis ST-300T closed-cycle helium cryostat. The sample temperature was determined using a Si-diode thermometer mounted on a copper block attached to the sample cell. The temperature was maintained using a Lakeshore Model 331 controller. A small quantity (less than 0.2 mbar) of He gas was introduced to the system to ensure thermal contact between the sample and the walls of the cell. Gas dosing was performed using a Micromeritics ASAP 2020 instrument. All gases were of research grade (> 99.99% purity). TPD was performed by first exposing the sample to a known amount of $H_2$ at a desired load temperature (20 or 293 K). The sample was then cooled at 5 K/min to a base temperature of 20 K. At this temperature, virtually all hydrogen was adsorbed. In all cases the

sample was maintained at the base temperature for at least 30 min. The sample was then heated at 5 K/min while measuring the evolving gas using a Hiden Analytical "Lo MASS" series quadrupole mass spectrometer. The instrument is optimized for quantifying low mass species and has a base operating pressure of $10^{-9}$ Torr when used in conjunction with a low-pressure capillary orifice.

Temperature programmed desorption (TPD) data utilizing excess $H_2$ were collected at the National Renewable Energy Laboratory (NREL) using a custom-built apparatus that allows for identification and quantification of effluent gases. Samples may be exposed to hydrogen (99.9999%) at pressures up to 1000 Torr, and the system can achieve pressures as low as $10^{-9}$ Torr. The TPD system is equipped with a mass spectrometer with detection range of 0−100 atomic mass units to detect impurities present in materials both during degas and after hydrogen exposures. In this work, the sample was initially degassed to 423 K, dosed and equilibrated over 0.4 Torr $H_2$ at either 76 K (the boiling point of nitrogen in Golden, CO) or room temperature. The sample was then cooled with liquid $N_2$, evacuated, and upon heating at 15 K/min, the $H_2$ desorbed was measured.

**Hydrogen adsorption kinetics.** Adsorption kinetics measurements were performed at 276, 285, 295, and 300 K on a Micromeritics 3Flex gas sorption analyzer. Data at each temperature were collected in triplicate. A Julabo F32 water circulator was used as the isothermal bath. The manifold pressure and material uptake were monitored as a function of time (0.5 Hz) using the DataMonitor software from Micromeritics. A sample of activated $Cu^{I}$-MFU-4*l* (0.0889 g) was loaded into a glass sample tube capped with a transeal. A glass rod of approximately equal length was inserted so as to minimize the free space within the tube. Free space measurements were performed using He at the analysis temperature. Following complete evacuation of He, the samples were dosed with 2.0 mmol/g of $H_2$. When adsorption over the framework sample was monitored, nearly all adsorption was seen to occur within 6 s. Accordingly, the timepoints between 0–6 s were utilized to construct plots of coverage versus time. The transient adsorption data were found to be modeled very well by the first-order Langmuir rate law (also known as the Lagergren expression)[32]:

$$\frac{d\theta_t}{dt} = k_1(\theta_e - \theta_t)$$

in which $\theta_t$ is the fractional coverage at a given time $t$, $\theta_e$ is the fractional coverage at equilibrium, and $k_1$ is the first-order rate constant. Upon integration, this expression becomes:

$$\ln(\theta_e) - \ln(\theta_e - \theta_t) = k_1 t$$

As shown in Supplementary Fig. 10, the transient adsorption data obtained for $Cu^{I}$-MFU-4*l* conform very well to this expression. Note that inferior fits were obtained using a second-order Langmuir kinetic expression. For an in-depth discussion on the merits of the first- and second-order kinetic expressions, see Ref. *32*. The mean of the three rate constants determined for each run at a given temperature was used to calculate the activation barrier $E_a$ using the Arrhenius expression:

$$k_{obs} = Ae^{\frac{-E_a}{RT}}$$

where $k_{obs}$ is the mean rate constant measured at each temperature $T$ and $A$ is the pre-exponential constant. The rate constants determined at 276, 285, 295, and 300 K are 0.4975 $s^{-1}$,0.5741 $s^{-1}$, 0.6435 $s^{-1}$ and 0.0.6836 $s^{-1}$, respectively. This yields an activation energy $E_a$ of 9.0 kJ/mol (Supplementary Fig. 15).

**Density Functional Theory calculations.** Calculations were performed using a pentanuclear cluster model that represents the metal–organic framework building unit, where the $btdd^{2-}$ ligands have been truncated to benzotriazolates. The central octahedral $Zn^{2+}$ is surrounded by four metals in trigonal coordination environments. Two of these metals are $Zn^{2+}$ and are capped with a charge-balancing chloride. The other two metal sites are three-coordinate $Cu^{+}$ centers. See the supplementary text for an extended description of the methods utilized in the calculations reported herein.

**Cu L-edge X-ray absorption spectroscopy.** Soft X-ray spectroscopy measurements at energies near the Cu L-edge were performed at bending magnet beamline 6.3.2 at the Advanced Light Source, Lawrence Berkeley National Laboratory. $H_2$ gas dosing experiments made use of a custom-built gas cell and similar apparatus as previously described[52-54]. Samples were deposited on X-ray transparent 150 nm thick, 2.0 mm × 2.0 mm silicon nitride windows supported by a silicon frame (Silson Ltd.). To improve adhesion of the framework to the substrate, polystyrene ($M_w$ = 350 kg/mol, $M_n$ = 170 kg/mol) was dissolved in toluene at a concentration of 20 mg/mL and spin coated on top of the silicon nitride windows (2,000 rpm, 40 s) to form a thin polystyrene film (polystyrene exhibits minimal absorption near the Cu L-edge). Pre-activated $Cu^{I}$-MFU-4*l* was suspended in *n*-hexane in an argon-filled glovebox, sealed in a borosilicate vial, removed from the glovebox and sonicated for 5 min. The vial was then brought back into the glovebox, and the framework was drop-cast atop the polystyrene-coated $Si_3N_4$ windows. After evaporation of the hexane, the window was heated *in vacuo* at 80 °C (approximately 50 mTorr) for at least 2 h. Samples were then sealed in vials and transferred to a $N_2$-filled glovebox where they were loaded into the gas cell and sealed before bringing to the beamline. The beamline X-ray energy was calibrated to the edge step of a Cu filter, which was set to 1.3293 nm (932.7 eV). Once attached to the beamline, the sample was pumped and kept at high vacuum (~$10^{-7}$ Torr) for at least 30 min before any NEXAFS spectra were collected. A transmission NEXAFS spectra of the activated framework was collected before any exposure to $H_2$ gas. Following collection of NEXAFS spectra of the activated material, $H_2$ gas (Praxair, Ultra High Purity grade) was slowly introduced in the gas cell and spectra were collected *in situ* at $H_2$ pressures of 200, 350, 500, 750, and 1000 mbar. After gas dosing, the gas cell was pumped back down to high vacuum and a final spectrum was measured to ensure reversibility. A bare polystyrene-coated silicon nitride window was used for background correction. For normalization, a line was regressed to the pre-edge region and a polynomial regressed to the post-edge region using the Athena software package[55]. The sample position was not moved during measurement to minimize effects due to spatial and thickness inhomogeneity of the drop-cast sample.

**Diffuse reflectance infrared spectroscopy (DRIFTS) measurements.** Infrared spectra were collected using a Bruker Vertex 70 spectrometer equipped with a glowbar source, KBr beamsplitter, and a liquid nitrogen cooled mercury-cadmium-telluride detector. A custom-built diffuse reflectance system with an IR-accessible gas dosing cell was used for all measurements.

Sample temperature was controlled by an Oxford Instruments OptistatDry TLEX cryostat, and sample atmosphere was controlled by a Micromeritics ASAP 2020Plus gas sorption analyzer. In a typical experiment, activated framework material was dispersed in dry KBr (10 wt %) in an argon-filled glovebox and evacuated at room temperature overnight. Spectra were collected *in situ* under UHP-grade $H_2$ and $D_2$ (99.6 atom % D, Sigma-Aldrich) at 4 $cm^{-1}$ resolution continually until equilibrium was observed.

**Data availability**

The supplementary information contains additional experimental details on some of the measurements reported herein, as well as supplementary figures and tables. Crystallographic data are available free of charge from the Cambridge Crystallographic Data Centre (CCDC). The CCDC numbers for the powder neutron diffraction structures reported here are 1987754-1987758.

**References**


46. Armarego, W. L. F. & Chai, C. L. L. *Purification of Laboratory Chemicals*, (Elsevier, 2003).

47. Larson, A. C. & Von Dreele, R. B. General Structure Analysis System (GSAS), Los Alamos National Laboratory Report LAUR, **2000**, 86–748.

48. Toby, H. B. EXPGUI, a graphical user interface for GSAS. *Appl. Cryst.* **34**, 210–213 (2001).

49. Le Bail, A. Whole powder pattern decomposition methods and applications: A retrospection. *Powder Diffr.* **20**, 316–326 (2005).

50. Morcombe, C. R. & Zilm, K.W. Chemical shift referencing in MAS solid state NMR. *J. Mag. Res.* **162**, 479–486 (2003).
51. Rossin, A., Chierotti, M. R., Giambastiani, G., Gobetto, R. & Peruzzini, M. *CrystEngComm* **14**, 4454–4460 (2012).

52. Drisdell, W. S. & Kortright, J. B. Gas cell for *in situ* soft X-ray transmission-absorption spectroscopy of materials. *Rev. Sci. Instrum.* **85**, 074103 (2014).

53. Drisdell, W. S. *et al.* Probing adsorption interactions in metal–organic frameworks using X-ray spectroscopy. *J. Am. Chem. Soc.* **135**, 18183–18190 (2013).

54. Drisdell, W. S. *et al.* Probing the mechanism of $CO_2$ capture in diamine-appended metal–organic frameworks using measured and simulated X-ray spectroscopy. *Phys. Chem. Chem. Phys.* **17**, 21448–21457 (2015).

55. Ravel, B. & Newville, M. Athena, Artemis, Hephaestus: Data analysis for X-ray absorption spectroscopy using ifeffit. *J. Synchrotron Radiat.* **12**, 537–541 (2005).

**Acknowledgements**

The authors gratefully acknowledge research support from the Hydrogen Materials – Advanced Research Consortium (HyMARC), established as part of the Energy Materials Network under the U.S. Department of Energy, Office of Energy Efficiency and Renewable Energy, Fuel Cell Technologies Office, under Contract Number DE-AC02-05CH11231. X-ray absorption spectroscopy measurements were performed at Beamline 6.3.2 of the Advanced Light Source, Lawrence Berkeley National Laboratory, supported by the Director, Office of Science, Office of Basic Energy Sciences, of the U.S. Department of Energy under Contract DE-AC02-05CH11231. H.A.E and B.A.T. were supported by an NRC/NIST Research Fellowship and a NIST Director's Postdoctoral Fellowship, respectively. G.M.S. and W.S.D. were supported by the Center for Gas Separations Relevant to Clean Energy Technologies, an Energy Frontier Research Center supported by the U.S. Department of Energy, Office of Science, Office of Basic Energy Sciences, under Award DE-SC0001015. S.A.F. thanks the U.S. National Science Foundation for funding (CHE-1565961). L.M.F. thanks the Alexander von Humboldt Foundation for a Feodor Lynen Postdoctoral Research Fellowship. J.B. acknowledges the Deutsche Forschungsgemeinschaft (DFG) for a Postdoctoral Research Fellowship. Certain commercial equipment, instruments, or materials are identified in this document. Such identification does not imply recommendation or endorsement by the National Institute of Standards and Technology, nor does it imply that the products identified are necessarily the best available for the purpose. We thank Dr. Katie R. Meihaus for editorial assistance, and Dr. Hiroyasu Furukawa and Dr. T. David Harris for helpful discussions.

**Author contributions**

B.R.B. and J.R.L. conceptualized the project and wrote the paper with input from all coauthors. B.R.B. performed all synthetic manipulations and isotherm data collection. H.A.E, B.A.T., J.D.T., and C.M.B. collected and analyzed the powder neutron diffraction data. G.M.S. and W.S.D. collected and analyzed the L-edge X-ray absorption spectra. H.Z.H.J. and J.B. collected and analyzed the infrared spectroscopy data. R.C. and M.H.-G. carried out and analyzed all computational work. D.B., T.J.H., M.B.M., K.E.H., T.G., and S.A.F. collected and analyzed the temperature-programmed desorption data. M.N.D. and B.R.B. collected and analyzed the adsorption kinetics data. L.M.F. and J.A.R. collected and analyzed the solid-state $^{13}C$ NMR spectroscopy data.

**Competing interests**

The authors have no competing interests to declare.

Supplementary Information for the paper entitled:

# Observation of an intermediate to $H_2$ binding in a metal–organic framework

Brandon R. Barnett[1,2], Hayden A. Evans[3], Gregory M. Su[4], Henry Z. H. Jiang[1,2], Romit Chakraborty[1,2], Didier Banyeretse[5], Tyler J. Hartman[5], Madison B. Martinez[6], Benjamin A. Trump[3], Jacob D. Tarver[3], Matthew N. Dods[7], Lena M. Funke[1,7], Jonas Börgel[1], Jeffrey A. Reimer[2,7], Walter S. Drisdell[4], Katherine E. Hurst[6], Thomas Gennett[6,8], Stephen A. FitzGerald[5], Craig M. Brown[3,9], Martin Head-Gordon[1,4], and Jeffrey R. Long[1,2,7*]

## Table of Contents

## I. Supplementary Text

**Powder neutron diffraction data collection specifics**. The activated bare material was measured at the base temperature (7 K) for sufficient time to be able to perform high quality Rietveld refinements. Space group $Fm\bar{3}m$ was chosen based on an analogous previously reported structure obtained from X-ray diffraction[1]. A crystallographic model was constructed with a 55:45 composition of Cu and Zn in the periphery of the inorganic cluster (based on ICP data), and where the Zn position is independent of that of the Cu. All tetrahedral Zn sites were modeled as being capped with a chloride ligand based off of our elemental analysis, $^{13}C\{^{1}H\}$ ssNMR, and FT-IR measurements. We investigated alternative models that either replaced these chlorides with formate ligands, or incorporated a disordered mixture of chloride and formate ligands, although these models provided inferior agreement with the diffraction data and were accordingly abandoned. Importantly, the Fourier difference map from our solution for the bare framework (Supplementary Fig. 6) shows no residual density anywhere in the viscinity of the chloro ligands. A small amount of positive density is found at the very center of the pores, which is an artifact of the data. The residual density around the triazolate N atoms likely arises from the Cu/Zn compositional disorder, as the precise coordination environments of $Zn^{2+}$ and $Cu^{+}$ in this system vary from one another (Supplementary Fig. 16).

Given the proximity of the zinc-bound chloro ligands to $D_2$ binding sites I and I*, the chlorine $U_{iso}$ for all subsequent models was fixed to the value obtained from the bare model refinement for consistency between experiments. While this $U_{iso}$ value of 0.159(34) is larger than those of other framework atoms, this is not particularly surprising given that the monodentate nature of $Cl^{-}$ may impart it with substantially more vibrational freedom. Stoichiometric gas dosing measurements were performed with approximately 0.75 $D_2$:Cu, as well as a higher dosing (3.50 $D_2$:Cu) to confirm $D_2$ positions. After establishing an activated structural model, Fourier difference maps were obtained from the higher $D_2$ dosing refinement to guide $D_2$ location assignment within the crystal structures.

Data sets were collected while heating the bare material from 10 to 300 K to determine the effects of temperature on the lattice parameters (Supplementary Fig. 9). These parameters were extracted using the Le Bail whole pattern fitting method[2]. Between 100 and 250 K the average negative thermal expansion (NTE) coefficient, α, is $-9.6 \times 10^{-6}$ $K^{-1}$, slightly smaller than observed in MOF-5 ($-16 \times 10^{-6}$ $K^{-1}$ to $-10 \times 10^{-6}$ $K^{-1}$)[3]. Data sets were then collected with a sample of framework dosed with 0.75 $D_2$:Cu at 77 K that was then rapidly cooled to a base temperature of 7 K. Quick scans (1 hour) at select temperatures were collected during heating of this sample to 300 K and then during cooling to 7 K. Lattice parameters were again extracted using the Le Bail whole pattern fitting method. It should be important that dosed samples were not necessarily at equilibrium during data collected for lattice parameter determination, especially for the low temperature points taken upon heating from 7 K. Between base temperature (7 K) and 75 K there is a significant contraction of $-6.05 \times 10^{-6}$ $K^{-1}$, corresponding to adsorption of $D_2$ at Site I. Between 100 and 175 K, the material displays NTE behavior that mirrors the bare framework. Beginning at approximately 175 K, spontaneous desorption begins to occur and the lattice parameter increases, beginning to approach that of the bare framework at the maximum temperature of 300 K. As $D_2$ is desorbed from the

sample, the crystal returns back to its intrinsic 'bare' lattice parameter. Cooling below 100 K shows an open hysteretic loop due to the fact that $D_2$ remains adsorbed at Site I.

**Intricacies of sample preparation for temperature-programmed desorption experiments utilizing sub-stoichiometric $H_2$ dosing**. The presence of the new TPD desorption peak at a lower temperature than that corresponding to chemisorption is demonstrated in Fig. 2 and Supplementary Fig. 10. As shown in Supplementary Fig. 11, the presence of this peak is dependent upon both the compaction of the material within the cell and the amount of material utilized. The orange data was obtained using 47 mg of material compacted within the TPD cell. This is the maximum amount of material that could fit within the cell. If less material is used but is still manually compacted prior to measurements, the new desorption event manifests as a shoulder on the low-*T* side of the chemisorption peak. If compaction is completely omitted, only a single desorption peak is observed. The amount of material utilized also has a noticeable effect on the temperature at which the peak maxima occur. When using a small amount of material (*ca.* 10 mg), as was done for the red and blue lines, the desorption maximum for the chemisorption peak occurs around 210–220 K. However, when the cell is filled completely with material, this peak shifts to a higher temperature. These effects were verified to be reproducible. We attribute the temperature shift to the fact that desorbing $H_2$ will, on average, undergo more desorption/adsorption events when more material is packed into the cell. This should increase time between the initial desorption event and egress from the cell for a given $H_2$ molecule.

**Details of density functional theory calculations.** Optimal coordinates were obtained for the bare framework with two open $Cu^+$ metal sites and for the hydrogen-loaded framework. Geometry optimization was performed with $\omega$B97M-V[4], a combinatorically optimized, range-separated hybrid, meta-GGA functional with VV10 non-local correlation[5]. Geometries were optimized with the CRENBL basis, and fit-CRENBL effective core potential (ECP)[6] for reasons of economy. The CRENBL basis with the fit-CRENBL ECP employs a 6-311G* basis for H atoms and its size for heavy atoms lies in between LANL2DZp and SDB-cc-pVTZ[7]. Effective core potentials employed in the basis CRENBL with fit-CRENBL ECP are a refinement of the "shape consistent" effective potential procedure of Christiansen, Lee, and Pitzer[8] and have been employed in numerous molecular calculations[9-12] that have attested to their reliability when compared to all-electron computations. In terms of basis cardinality for valence shell electrons (X), the CRENBL basis is positioned in between double (X=D) and triple (X=T) zeta basis sets for heavy atoms, and for hydrogen it employs the triple zeta valence polarized basis 6-311G*. Electronic structure computations were performed in Q-Chem 5.1[13].

All framework coordinates were relaxed, and geometry optimization performed in delocalized internal coordinates as developed by Baker *et al.*[14]. Self-Consistent Field (SCF) convergence at each cycle of the geometry optimization procedure had a convergence threshold of $10^{-8}$ a.u. for the DIIS error. The initial guess for each SCF cycle was provided from converged electron densities on each fragment, the $Cu^+$-containing MFU-4*l* node and the binding molecular hydrogen. Energy minima corresponding to the bare and hydrogen-bound framework were obtained using Baker's

eigenvector-following (EF) algorithm[15] that is capable of locating transition states on the molecular potential energy surface. Energy minima at optimal geometries were confirmed by frequency analysis at $\omega$B97M-V/CRENBL/fit-CRENBL ECP level of theory by the absence of any imaginary frequencies. The fully optimized cluster geometries containing zero, one, and two Cu-adsorbed $H_2$ molecules are shown in Supplementary Fig. 16-18. Molecular hydrogen binding causes a significant geometric distortion in framework geometry. Introduction of hydrogen causes $Cu^+$ to drift away from the octahedral $Zn^{2+}$ at the center of the node resulting in increased pyramidalization of the $Cu^+$ coordination environment.

To compare the effect of framework relaxation on hydrogen binding to a rigid framework, geometry optimization was also performed with all framework coordinates frozen, and only those of the binding molecular hydrogen relaxed. As expected, freezing the node results in attenuated interactions of $H_2$ with the open copper site as evidenced by an elongated Cu–$H_2$ distance and a shorter H–H separation (Supplementary Fig. 19).

Single-point calculations were performed at the optimal geometries with the $\omega$B97M-V functional with a more complete basis set comprising Karlsruhe triple-$\zeta$ basis def2-TZVPPD on Cu and the binding $H_2$ molecule and def2-SVP elsewhere (referred to hereon as def2-TZVPPD(def2-SVP))[16]. With the introduction of this customized basis, 2$f$ and 1$g$ polarization functions were added at the Cu site along with the addition of diffuse functions on Cu and the binding $H_2$ molecule. The DIIS convergence threshold for self-consistent field iterations was set at $10^{-7}$ a.u.

Energy decomposition analysis (EDA) methods are a useful set of tools for unraveling the origin of intermolecular interactions[17-19]. As the hydrogen molecule approaches the open metal site in an $Cu^I$-MFU-4$l$ node, its interaction with the framework can by decomposed into terms arising out of geometric distortion of the hydrogen molecule and the Cu-containing node ($\Delta E_{gd}$), electrostatic repulsion between frozen electron densities and nuclei on fragments ($\Delta E_{frz}$), dispersion interactions ($\Delta E_{disp}$), polarization ($\Delta E_{pol}$) and finally charge transfer between electron orbitals ($\Delta E_{ct}$). The total energy of binding can be written as the sum of contributing terms

$$\Delta E_{bind} = \Delta E_{gd} + \Delta E_{frz} + \Delta E_{disp} + \Delta E_{pol} + \Delta E_{ct}.$$

Table S2 lists each contribution for hydrogen binding to the framework. Compared are energy contributions for each term for the rigid and relaxed $Cu^I$-MFU-4$l$ node. Binding energy estimates in Supplementary Table 2 were obtained after accounting for basis set superposition error (BSSE)[20,21] with counterpoise corrections[22]. Note that the $\omega$B97M-V functional employed in this EDA incorporates non-local electron correlations designed to accurately capture dispersion interactions[5].

Covalent character of the bond between molecular hydrogen and $Cu^+$ was established by a large charge transfer term (−46.1 kJ/mol). A comparison of rigid versus relaxed node EDA measurements in Supplementary Table 2 reveals the effect of structural deformities on chemisorption and on the framework electronic structure. Binding energy substantially increased with more efficient charge transfer between hydrogen and the fully optimized node with the open $Cu^+$ site. While all nuclear coordinates of the node were completely relaxed in these simulations, in reality, each node of the framework is constrained by its linkage to adjacent nodes in the extended

framework, and 17.9 kJ/mol is most reasonably taken as an upper estimate for $\Delta E_{gd}$. Fully optimized nuclear modes of the node gave an estimate for total interaction energy ($\Delta E$) of 34.2 kJ/mol, which is in good agreement with the value of the binding enthalpy determined experimentally using DRIFTS.

The change in enthalpy on hydrogen binding was calculated under a rigid-rotor harmonic oscillator (RRHO) approximation. Following a frequency analysis at the equilibrium geometry for the bare and hydrogen bound MOF node, analytic partition functions for the harmonic oscillator and rigid rotor were used to calculate enthalpy and entropy changes at 298.15 K and 1.00 atm. Supplementary Table 3 compares enthalpy and entropy changes in the reaction obtained under the RRHO approximation at ωB97M-V/CRENBL/fit-CRENBL ECP level of theory to experimentally measured values from DRIFTS. A total of 59 nuclear modes were found between the frequency range 18–300 $cm^{-1}$ for the hydrogen-loaded node, many of which were coupled to the bound hydrogen. While the overall agreement is excellent, sources of error in the computational enthalpy estimate reported in Table S3 stem from the RRHO approximation and possible overestimation of geometric distortion energy of the node ($\Delta E_{dg}$) on allowing all nuclear modes in the MOF fragment to relax.

Constrained optimizations were performed to search for a barrier to adsorption. A smaller cluster bearing parent triazolate ($[N_3C_2H_2]^-$) instead of benzotriazolate ligands was employed to facilitate convergence to optimal nuclear configurations at each step. Constrained optimizations were performed in delocalized internal coordinates using the method of Lagrange multipliers implemented in Q-Chem by Baker[23]. The DIIS convergence threshold at each step of the optimization was $10^{-8}$ a.u. Convergence criteria for maximum absolute energy change, maximum gradient component, and maximum atomic displacement between two successive optimization cycles were $1\times10^{-7}$ a.u., $3\times10^{-4}$ a.u, and $12\times10^{-4}$ a.u., respectively. Fig. 4c shows the energy of the system comprising the $Cu^{I}$-MFU-4*l* node and molecular hydrogen as a function of Cu–$H_2$ distance at the B3LYP-D2/6-31++G**(6-31G*) level of theory. All nuclear coordinates of the framework were relaxed in these optimizations. A local minimum corresponding the weakly bound, physisorbed intermediate, labeled I*, appears at a distance of 2.43 Å from the Cu center.

Supplementary Fig. 20 offers a closer look at energy minima at the two basins as function of the angle $\theta$, defined here as the angle Cu–X–$H_y$ where X is the center of mass of molecular hydrogen and $H_y$ a tagged atom from the binding hydrogen molecule. The angle $\theta$ was found to increase from around 90° to 180° with increase in $d_{Cu–H2}$ in the constrained optimizations. Frequency calculations were run to confirm the veracity of local minimizers along the potential energy surface (PES) at geometries corresponding to configurations I and I*, yielding no imaginary frequencies. The DIIS convergence threshold was kept at $10^{-9}$ a.u. in frequency calculations. Based on this PES, the activation barrier to the strong-binding site is calculated to be 4.4 kJ/mol, which is smaller than the lower bound of 9.0 kJ/mol measured experimentally from adsorption kinetics measurements.

Constrained optimizations using the more complete basis set def2-TZVPPD(def2-SVP) lead to two observations (Supplementary Fig. 21). First, the chemisorption well runs deeper, which is congruent with the above EDA results where the binding energy at the site was found to be −34.2 kJ/mol after accounting for geometric distortion. Second,

the barrier obtained with B3LYP-D2/6-31++G**(6-31G*) disappears. Instead of a prominent activated intermediate along the chemisorption pathway, the PES smoothens, showing a marked shoulder in the region that had previously located an active intermediate. Flattening out of the PES curve with single point calculations in a larger basis demonstrates the difficulties inherent in trying to model the experimental behavior in the extended framework with a single cluster, which will necessarily possess more flexibility.

## II. Supplementary Figures

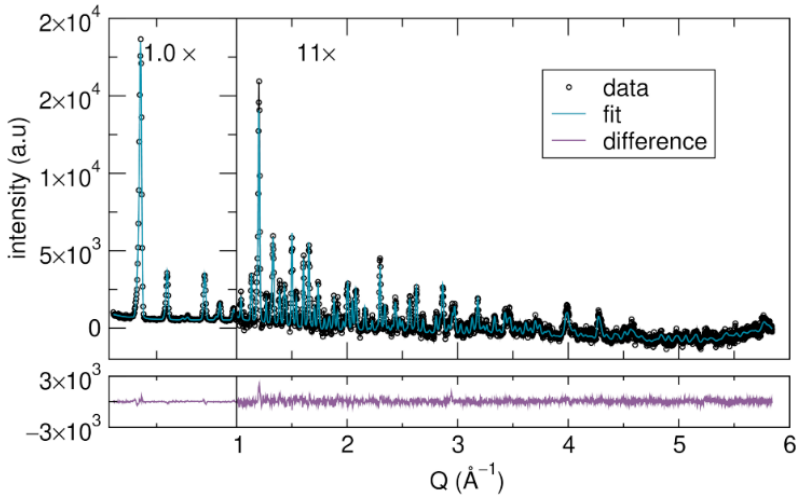


**Supplementary Fig. 1. Rietveld refinement data for activated $Cu^{I}$-MFU-4*l* at 7 K.** [NCNR, BT1], *Fm-3m*, $a$ = 31.2744(14) Å, $V$ = 30589(4) $Å^3$. Goodness-of-fit parameters: $\chi^2$ = 1.651; *wRp* = 4.57 %; *Rp* = 3.81 %. Values in parentheses and error bars indicate one standard deviation.

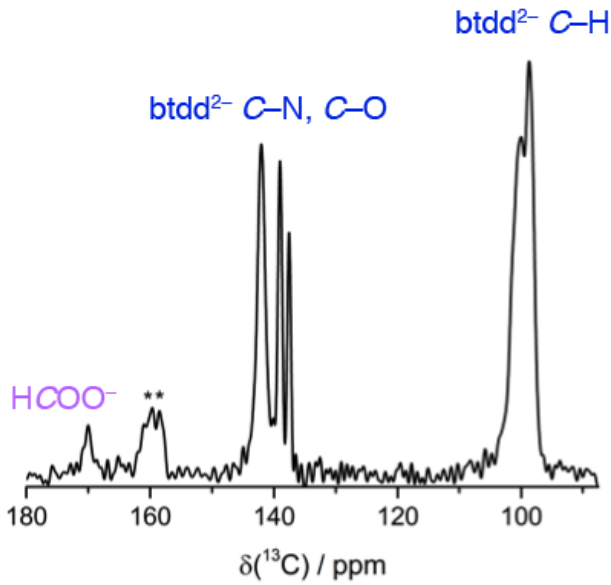


**Supplementary Fig. 2. Cross-polarization solid-state $^{13}C\{^1H\}$ NMR spectrum of activated $Cu^I$-MFU-4*l*.** The small peak at 170 ppm is consistent with the formate anion. The cluster of peaks centered around 159 ppm (labeled with **) are spinning sidebands.

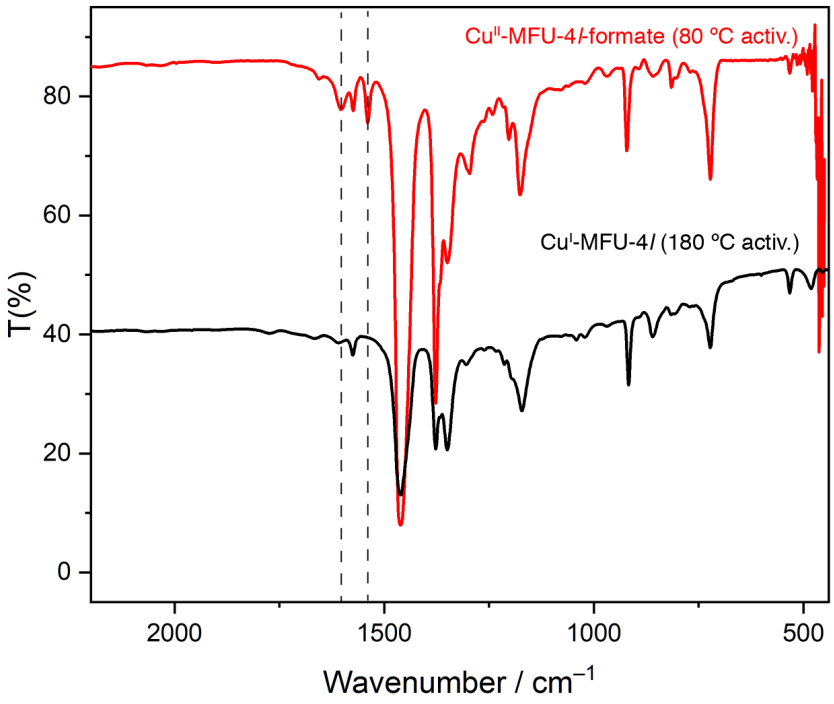


**Supplementary Fig. 3. FT-IR spectra of Cu-MFU-4*l* before and after thermal autoreduction of the formate moieties.** Spectra were measured in transmittance mode and prepared as nujol mulls under an Ar atmosphere. The formate-substituted framework containing $Cu^{2+}$ centers shows bands at 1540 and 1604 $cm^{-1}$ that were previously assigned as formate stretches[1]. Dashed lines are drawn through these peaks to guide the

eye. On heating the material *in vacuo* to 180 ºC for 3 h, reduction to $Cu^{I}$-MFU-4*l* occurs and the formate stretches are drastically reduced in intensity.

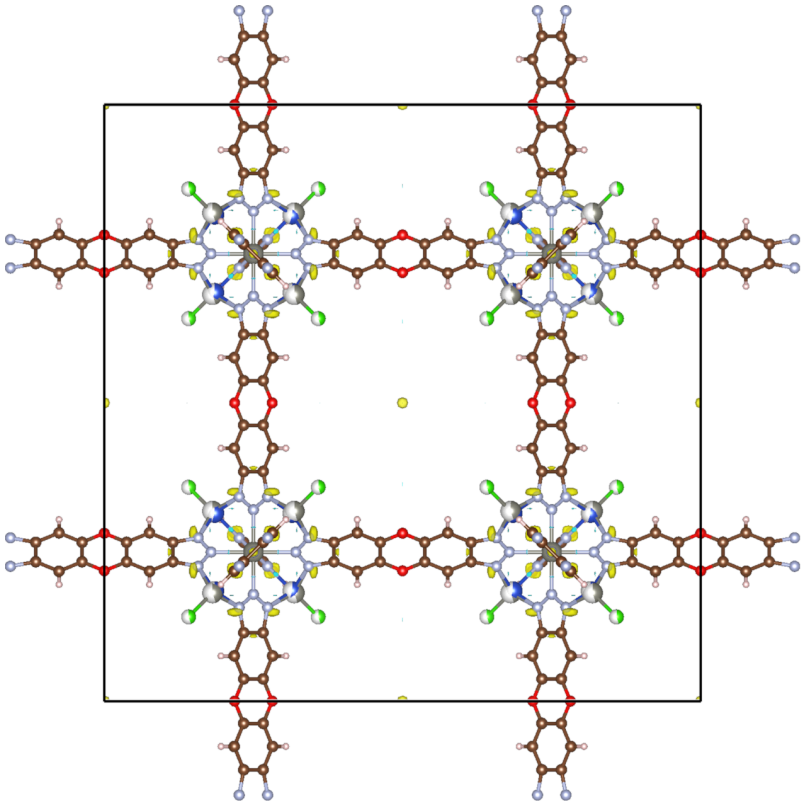

**Supplementary Fig. 4. Fourier difference map of from the refinement of PND data for bare $Cu^{I}$-MFU-4*l* collected at 7 K.** Importantly, no residual density (yellow) is seen in the vicinity of the Zn-bound chloro ligands, even at an appropriate isosurface level for small amounts of density to appear around the triazolate nitrogen atoms.

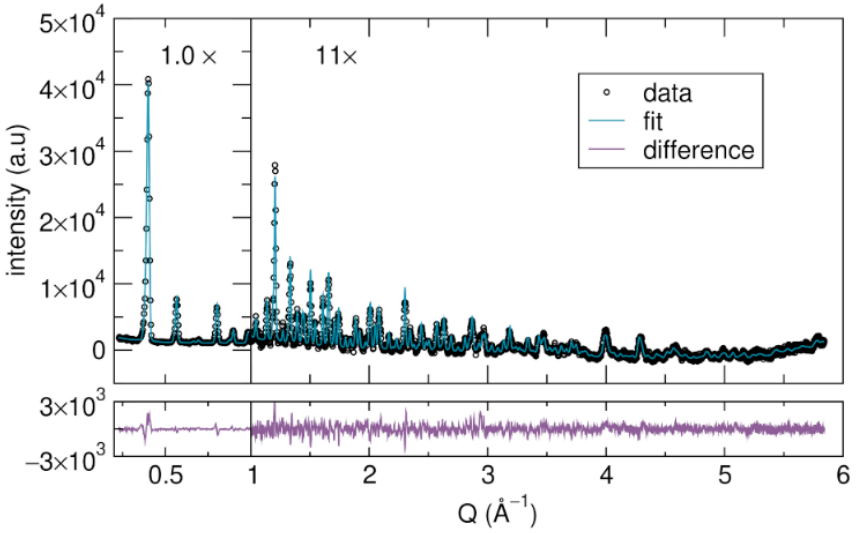


**Supplementary Fig. 5. Rietveld refinement data for $Cu^{I}$-MFU-4*l* dosed at 40 K with 0.75 $D_2$ per Cu, quenched and measured at 7 K.** [NCNR, BT1], *Fm-3m*, *a* = 31.2173(10) Å, *V* = 30421.8(28) $Å^3$. Goodness-of-fit parameters: $\chi^2$ = 1.448; *wRp* = 3.77 %; *Rp* = 3.29 %. Values in parentheses and error bars indicate one standard deviation.

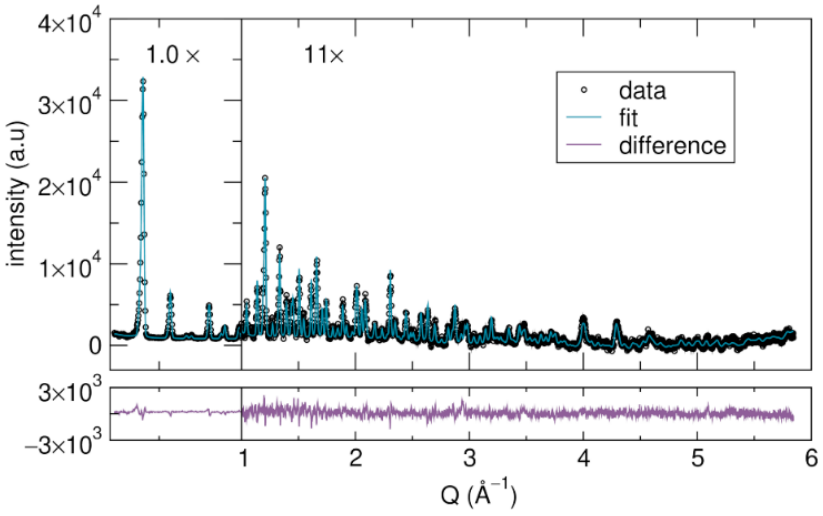


**Supplementary Fig. 6. Rietveld refinement data for Cu-MFU-4l dosed at 77 K with 0.75 $D_2$ per Cu, quenched, and measured at 7 K.** [NCNR, BT1], *Fm-3m*, *a* = 31.16521) Å, *V* = 30269.6(29) $Å^3$. Goodness-of-fit parameters: $\chi^2$ = 1.492; *wRp* = 4.18 %; *Rp* = 3.46 %. Values in parentheses and error bars indicate one standard deviation.

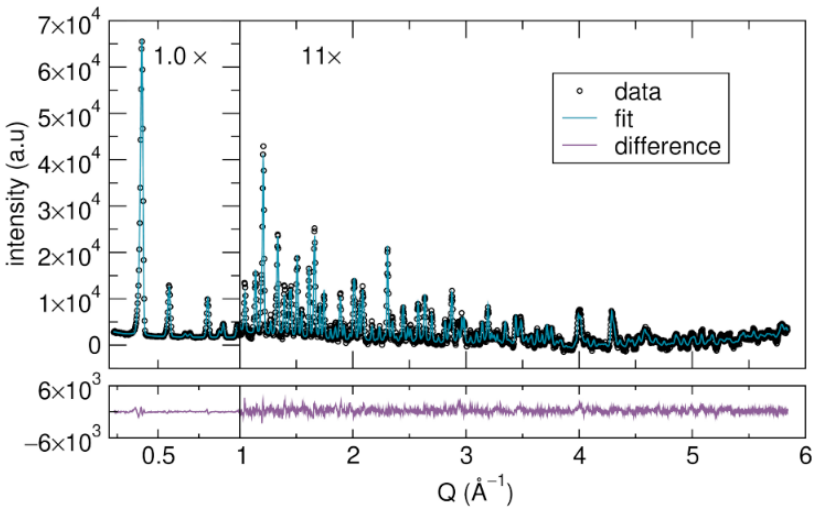


**Supplementary Fig. 7. Rietveld refinement data for Cu$^{I}$-MFU-4*l* dosed at 300 K with 0.75 $D_2$ per Cu, quenched and measured at 7 K.** [NCNR, BT1], *Fm-3m*, *a* = 31.1505(6) Å, *V* = 30227.1(18) Å$^3$. Goodness-of-fit parameters: $\chi^2$ = 1.675; *wRp* = 3.10 %; *Rp* = 2.53 %. Values in parentheses and error bars indicate one standard deviation.

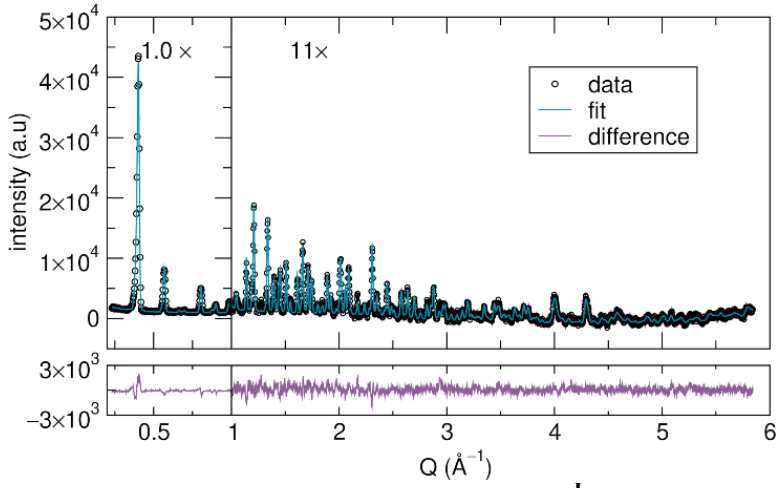


**Supplementary Fig. 8. Rietveld refinement data for Cu$^{I}$-MFU-4*l* dosed at 40 K with 3.5 $D_2$ per Cu, quenched and measured at 7 K.** [NCNR, BT1], *Fm-3m*, *a* = 31.1395(9) Å, *V* = 30194(25) Å$^3$. Goodness-of fit parameters: $\chi^2$ = 1.450; *wRp* = 3.85 %; *Rp* = 3.41 %. Values in parentheses and error bars indicate one standard deviation.

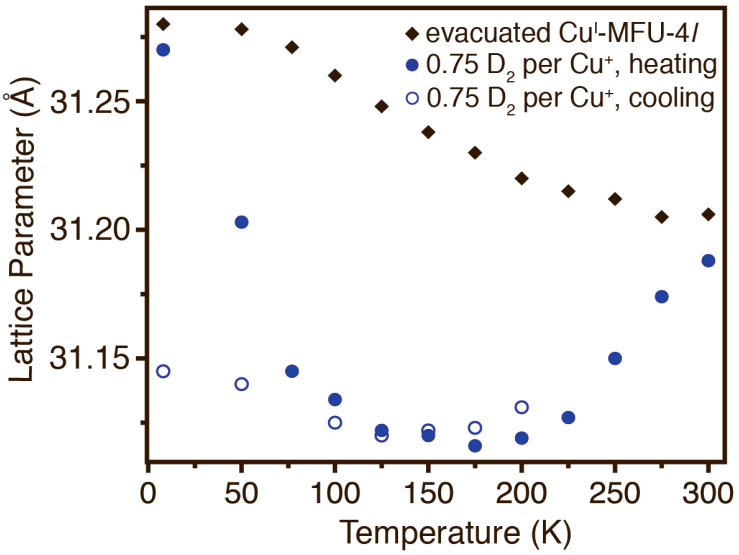


**Supplementary Fig. 9. Temperature dependence of the cubic lattice parameter *a*.** Data were obtained for an evacuated powder sample of $Cu^{I}$-MFU-4*l* upon heating from 7 K (black diamonds), following dosing with 0.75 $D_2$ molecules per Cu and heating at regular intervals (filled blue circles), and during subsequent cooling at regular intervals (open blue circles). Note that data was collected at fixed time points, and accordingly data points taken during heating of the $D_2$-dosed framework do not correspond to equilibrium states at low temperatures.

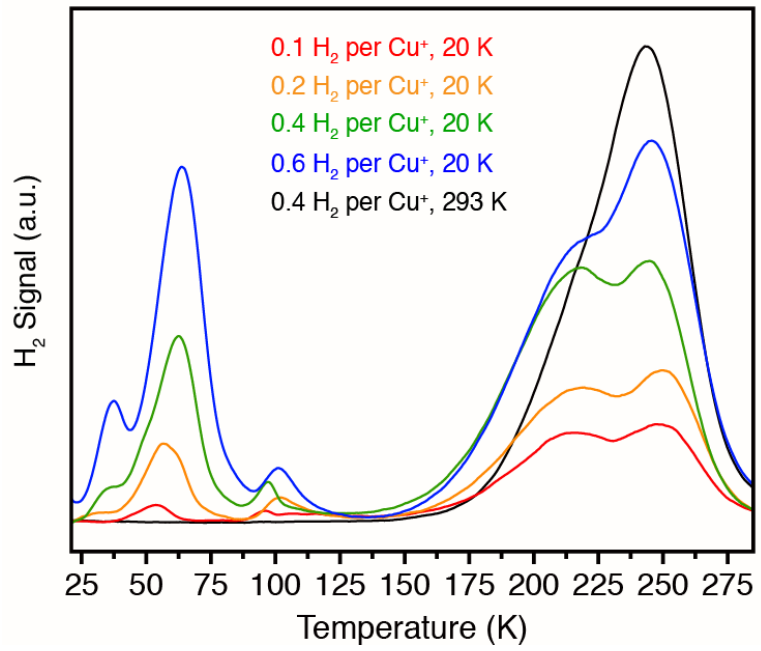


**Supplementary Fig. 10. TPD data collected following substoichiometric $H_2$ dosing.** The inset key shows the quantity of dosed $H_2$ per $Cu^+$ center and the temperature at which dosing was performed. A heating ramp rate of 5 K/min was used.

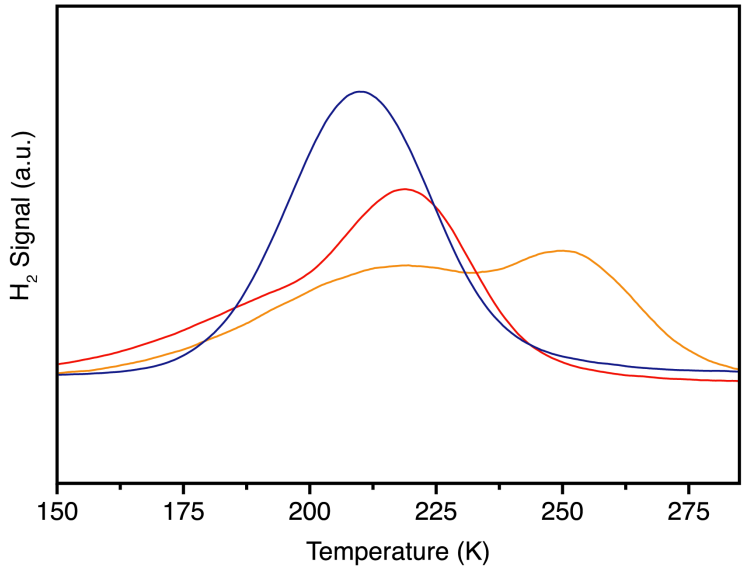


**Supplementary Fig. 11. TPD data collected following substoichiometric $H_2$ dosing and employing varying levels of framework compaction.** Samples were loaded with approximately 0.2 $H_2$ per $Cu^+$ at 20 K. The heating ramp rate was 5 K/min. The orange data was taken with the TPD cell completely filled with $Cu^I$-MFU-4*l* (this is the same data shown in Fig. 3). The data in red was collected with only about 1/4$^{th}$ of the material used for the orange data, but the framework was physically compacted within the cell. The blue data used the same amount of framework as the red data, but without the physical compaction.

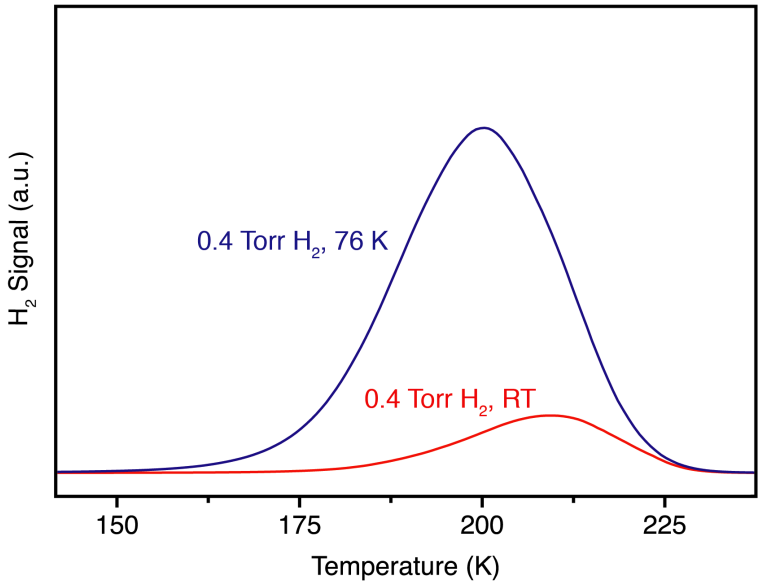


**Supplementary Fig. 12**. **TPD data collected following dosing with excess $H_2$**. Samples were dosed with an excess of $H_2$ (total pressure = 0.4 Torr) at either 76 K (the boiling point of $N_2$ in Golden, CO) or room temperature (RT). Samples were subsequently evacuated at 76 K for 30 min and then ramped at a constant rate of 15 K/min. The framework was not manual compacted within the sample cell.

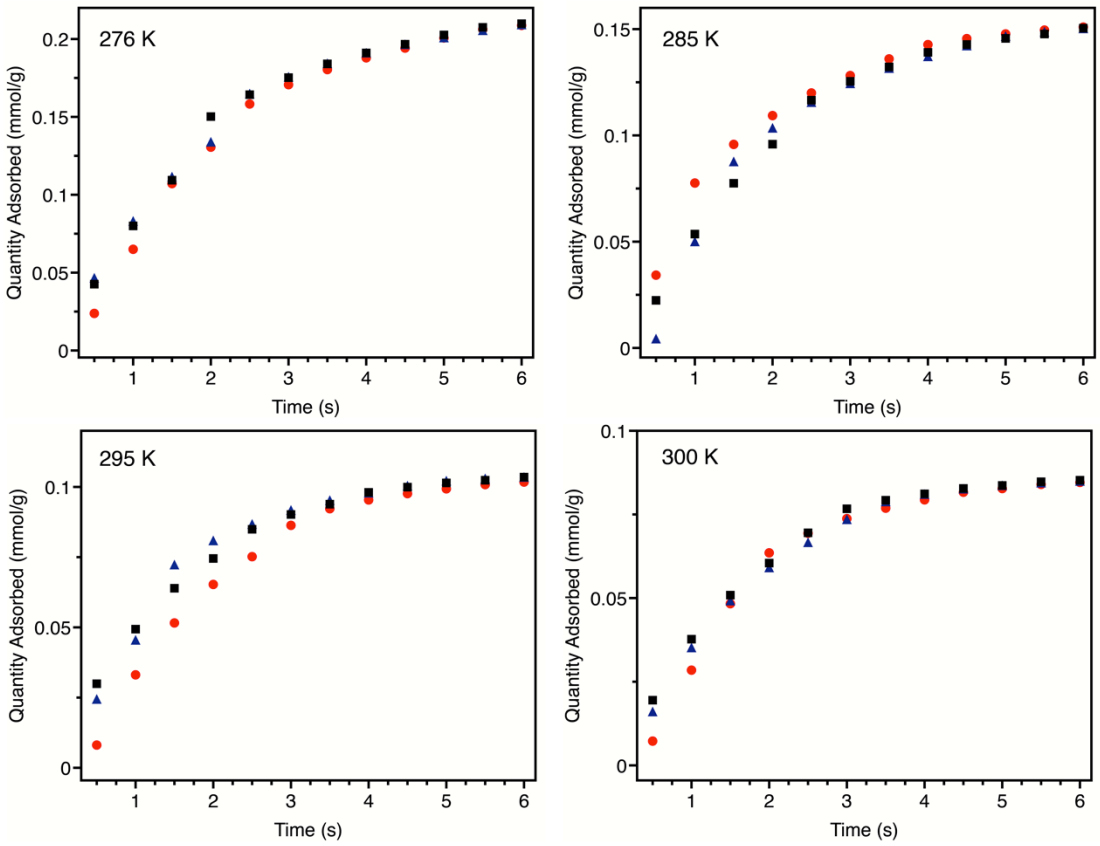


**Supplementary Fig. 13**. **Transient $H_2$ adsorption data for $Cu^I$-MFU-4*l*.** Data are shown for $T$ = 276, 285, 295 and 300 K.

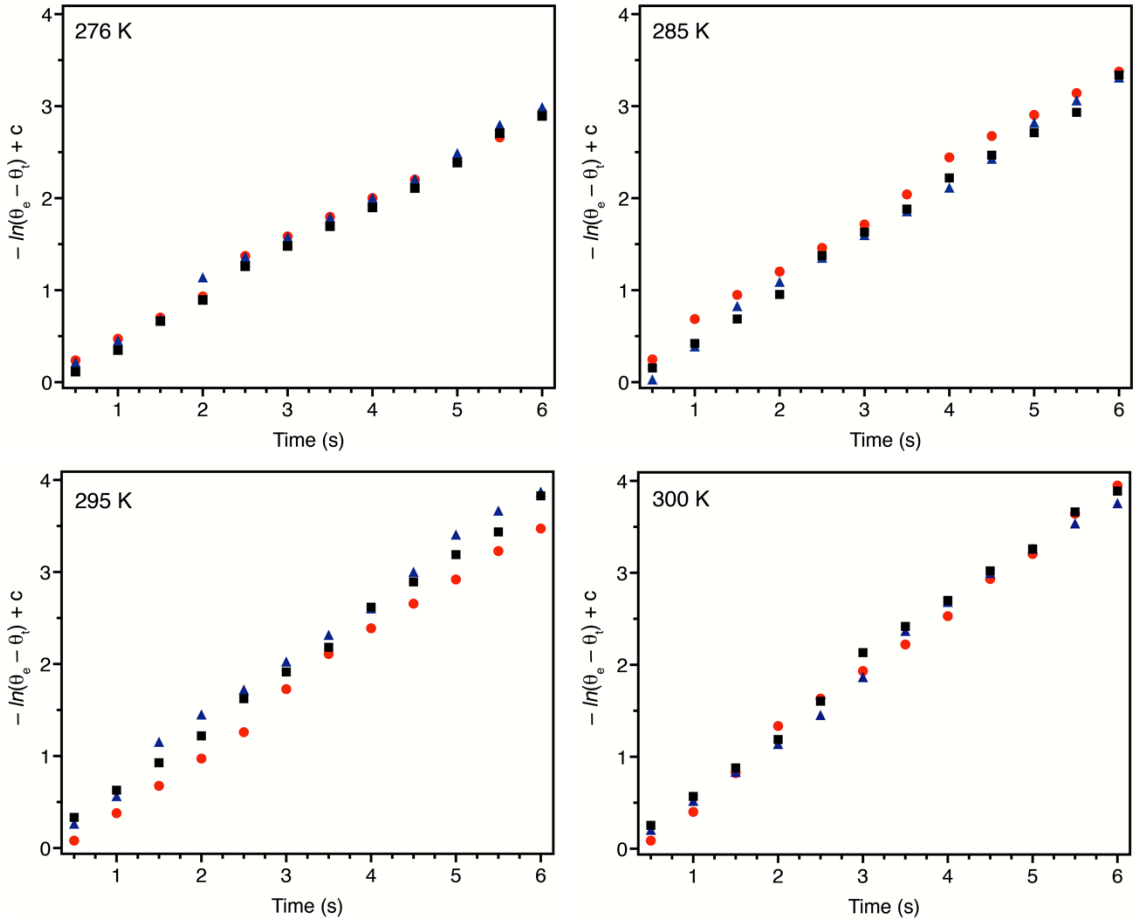


**Supplementary Fig. 14. Langmuir first-order kinetics plots**. Transient $H_2$ adsorption data fit to the Langmuir first-order rate law, where $\theta_e$ is the equilibrium coverage, $\theta_t$ is the coverage at time *t*, and c is a constant.

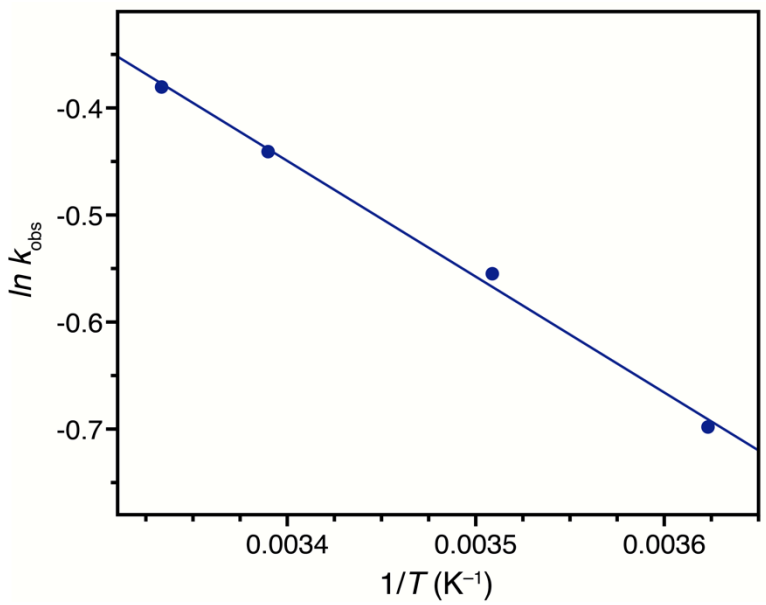


**Supplementary Fig. 15. Arrhenius plot of the hydrogen adsorption kinetics data.** Blue circles correspond to data points, while the blue line represents the least squares linear regression. The slope of this line is equal to $-E_a/R$, where $E_a$ is the activation energy and R is the ideal gas constant.

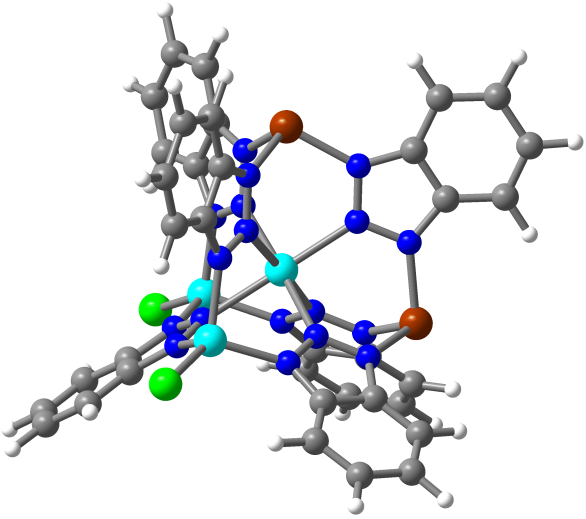

**Supplementary Figure 16. Optimized structure of cluster bearing no adsorbed $H_2$ molecules.** Brown, light blue, green, dark blue, grey, and white spheres represent copper, zinc, chloride, nitrogen, carbon, and hydrogen atoms, respectively. Selected distances and angles: Cu–Zn($O_h$) (mean) = 3.266 Å; Cu–N (mean) = 1.963 Å; Zn($O_h$)–N (mean) = 2.210 Å; N–Cu–N (mean) = 108.6°.

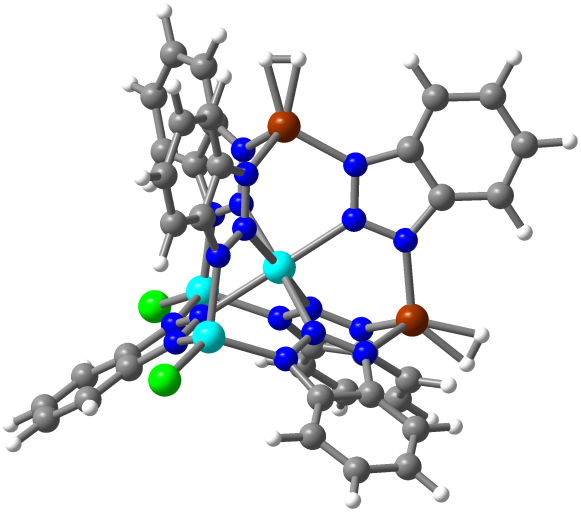

**Supplementary Figure 17. Optimized structure of cluster with both Cu centers bearing adsorbed $H_2$.** Brown, light blue, green, dark blue, grey, and white spheres represent copper, zinc, chloride, nitrogen, carbon, and hydrogen atoms, respectively. Selected distances and angles: Cu–Zn($O_h$) (mean) = 3.473 Å; Cu–N (mean) = 1.998 Å; Zn($O_h$)–N (mean) = 2.180 Å; Cu–H (mean) = 1.708 Å; H–H = 0.796 Å; N–Cu–N (mean) = 101.2°.

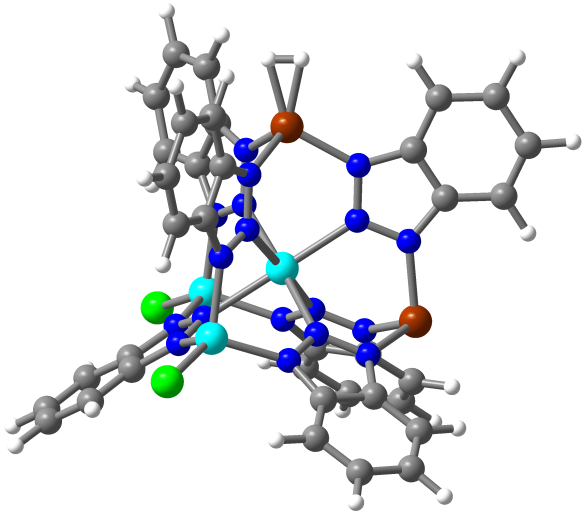

**Supplementary Figure 18. Optimized structure of cluster with one Cu center bearing adsorbed $H_2$.** The mean value of Zn($O_h$)–N distances is 2.194 Å. Brown, light blue, green, dark blue, grey, and white spheres represent copper, zinc, chloride, nitrogen, carbon, and hydrogen atoms, respectively. The mean value of Zn($O_h$)–N distances is 2.194 Å. Selected distances and angles that involve the three-coordinate $Cu^+$ center: Cu–Zn($O_h$) = 3.260 Å; Cu–N (mean) = 1.964 Å; N–Cu–N (mean) = 108.5°. Selected distances and angles that involve the $H_2$-ligated $Cu^+$ center: Cu–Zn($O_h$) = 3.487 Å; Cu–N (mean) = 1.999 Å; Cu–H (mean) = 1.703 Å; H–H = 0.797 Å; N–Cu–N (mean) = 101.0°.

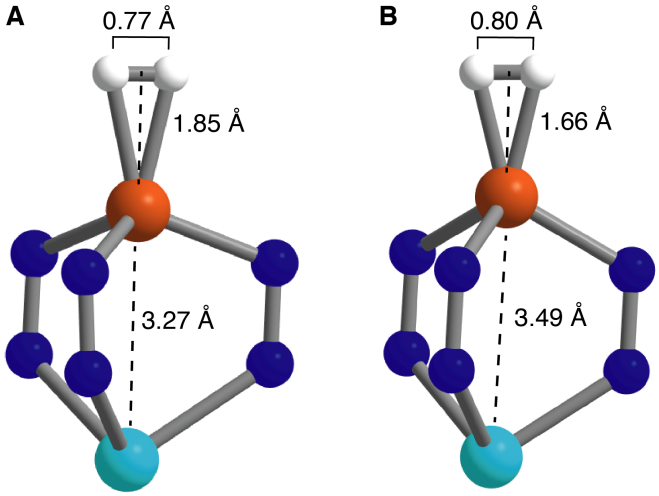


**Supplementary Fig. 19. Comparison of calculated cluster geometries.** (**A**) DFT optimized geometry for $H_2$ binding to a framework cluster wherein the cluster coordinates were frozen, and only the position of $H_2$ was allowed to relax. (**B**) DFT optimized geometry for $H_2$ binding to a framework cluster wherein all nuclear coordinates were allowed to fully relax. Note that these figures are truncated for clarity to only show a portion of the cluster used in these calculations. Calculations were carried out at the ωB97M-V/def2-TZVPPD(def2-SVP) level of theory.

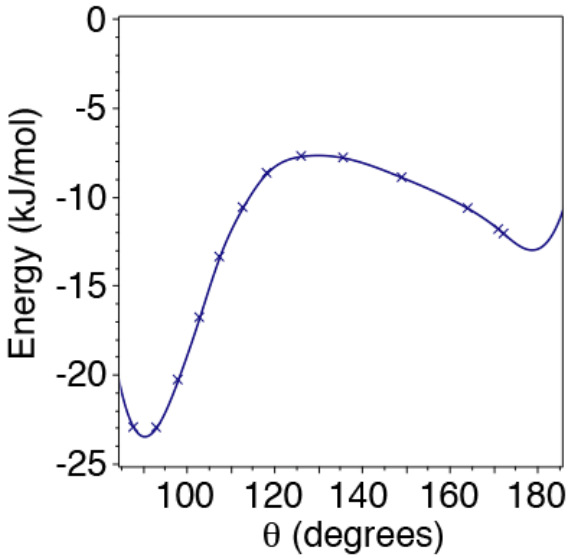


**Supplementary Fig. 20. Dependence of the angle Cu–X–$H_y$ ($\theta$) on the conversion from precursor state I* to chemisorbed I.** "X" corresponds to midpoint between the two H atoms, while $H_y$ is a tagged hydrogen atom. The local minimum at approximately 180° corresponds to the precursor state with $H_2$ binding to Cu in an end-on $\eta^1$ configuration, while the minimum at approximately 90° corresponds to the side-on $\eta^2$-bound chemisorbed species.

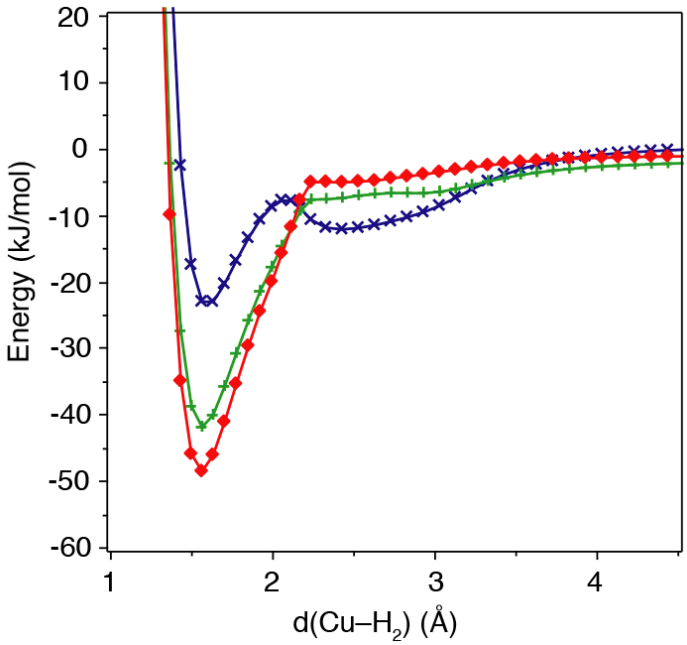


**Supplementary Fig. 21. Computed potential energy surface along the Cu–$H_2$ coordinate with different functional/basis-set combinations.** Blue data points correspond to B3LYP-D2/6-31++G**(6-31G*). Green data points correspond to B3LYP-D2/def2-TZVPPD(def2-SVP). Red data points correspond to ωB97M-V/def2-TZVPPD(def2-SVP).

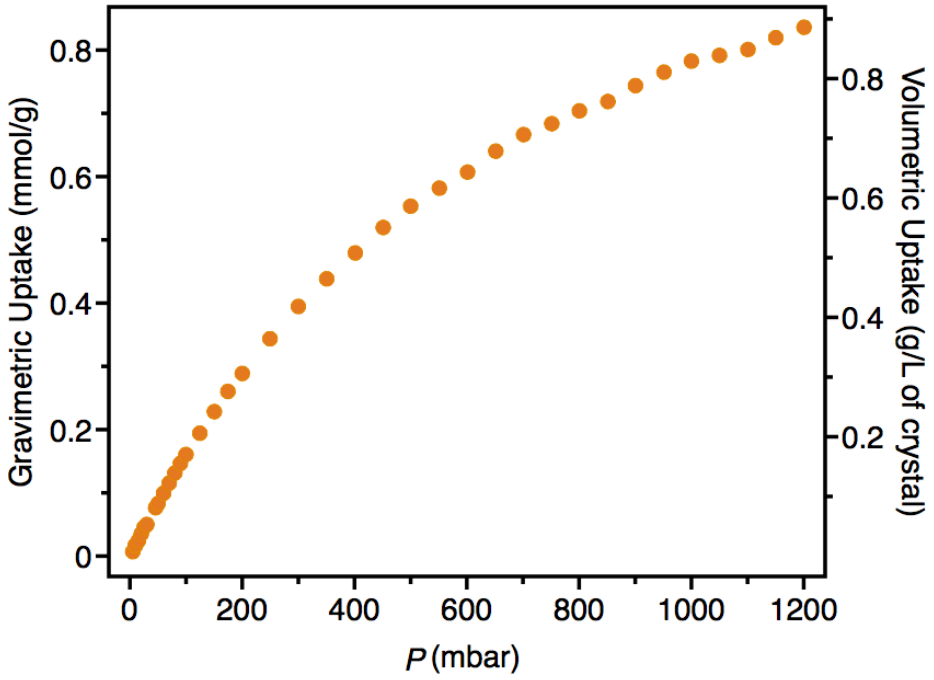


**Supplementary Fig. 22**. **Hydrogen adsorption isotherm (298 K) for Cu$^{I}$-MFU-4*l*.** An uptake of 1 $H_2$ per Cu corresponds to approximately 1.7 mmol/g. Volumetric uptake is calculated using the framework crystallographic density.

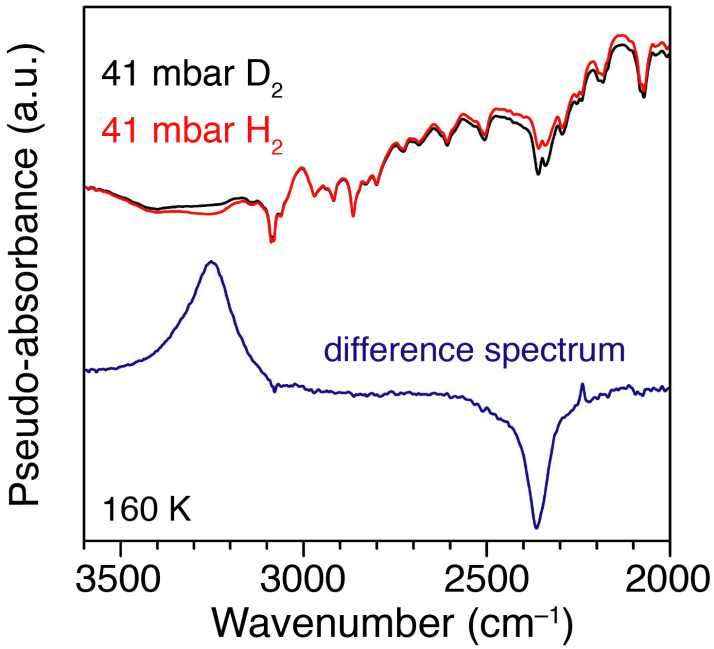


**Supplementary Fig. 23. DRIFTS spectra of Cu$^{I}$-MFU-4*l* under $H_2$ or $D_2$, and the resulting difference spectrum.** This subtraction procedure allows for the υ(H–H) and υ(D–D) features to be deconvoluted from framework-based vibrations.

## III. Supplementary Tables

**Table S1.** Crystallographic occupancies at sites I, I*, and II determined from powder neutron diffraction data obtained after dosing the bare framework with 0.75 equivalents of $D_2$ per Cu at the specified temperature. All diffraction data were collected at 7 K and the super-atom approach was used to model $D_2$ molecules as single D atoms (*23*). Converting between super-atom occupancies and $D_2$ occupancies involves dividing the former value by two. Subsequently dividing this value by the crystallographic occupancy of Cu (0.55) gives normalized $D_2$/Cu occupancies.

| Dosing $T$ | Amount Dosed | Site I D Super-atom Occupancy | Site I $D_2$/Cu Occupancy | Site I* D Super-atom Occupancy | Site I* $D_2$/Cu Occupancy | Site II D Super-atom Occupancy | Site II $D_2$/Cu Occupancy |
|---|---|---|---|---|---|---|---|
| 40 K | 0.75 $D_2$/Cu | 0.10(2) | 0.087(18) | 0.05(2) | 0.05(2) | 0.29(2) | 0.266(18) |
| 77 K | 0.75 $D_2$/Cu | 0.38(2) | 0.350(18) | 0.16(2) | 0.14(2) | – | – |
| 300 K | 0.75 $D_2$/Cu | 0.564(15) | 0.513(14) | 0.124(18) | 0.113(16) | – | – |
| 40 K | 3.5 $D_2$/Cu | 0.641(18) | 0.583(16) | 0.12(2) | 0.11(2) | 1.07(2) | 0.972(19) |

**Table S2.** Energy decomposition analyses delineating contributions to binding energy $\Delta E$ from geometric distortion, electrostatic interactions (frozen), dispersion, polarization, charge transfer and forward and back-donation between the Cu-containing node and molecular hydrogen at ωB97M-V/def2-TZVPPD (def2-SVP) level of theory. Two columns compare values for rigid versus relaxed $Cu^{I}$-MFU-4*l* node.

| Energy Contribution (kJ/mol) | Rigid | Relaxed |
|---|---|---|
| Geometric Distortion ($\Delta E_{gd}$) | 1.1 | 17.9 |
| Frozen ($\Delta E_{frz}$) | 51.9 | 63.9 |
| Dispersion ($\Delta E_{disp}$) | −23.3 | −25.4 |
| Polarization ($\Delta E_{pol}$) | −25.8 | −44.5 |
| Charge Transfer ($\Delta E_{ct}$) | −27.7 | −46.1 |
| Total (ΔE) | −23.8 | −34.2 |
| % Forward ($H_2$→Cu(I)) | 57% | 47% |
| % Back (Cu(I)→$H_2$) | 43% | 53% |

**Table S3.** Enthalpy and entropy change for molecular hydrogen binding to $Cu^{I}$-MFU-4l under RRHO approximation compared to experimentally measured values obtained via the DRIFTS setup.

| **Method** | ***T* (K)** | **Δ*H* (kJ/mol)** | **Δ*S* (kJ/mol)** |
|---|---|---|---|
| DRIFTS | 200–220 | −28(2) | −89(8) |
| RRHO/*ωB*97M-V/CRENBL | 298.15 | −30.1 | −105 |

## IV. References


1. Denysenko, D., Grzywa, M., Jelic, J., Reuter, K. & Volkmer, D. Scorpionate-type coordination in MFU-4*l* metal–organic frameworks: Small-molecule binding and activation upon the thermally activated formation of open metal sites. *Angew. Chem. Int. Ed*. **53**, 5832–5836 (2014).

2. Le Bail, A. Whole powder pattern decomposition methods and applications: A retrospection. *Powder Diffr.* **20**, 316–326 (2005).

3. Zhou, W., Wu, H., Hartman, M. R. & Yildirim, T. Hydrogen and methane adsorption in metal–organic frameworks: a high-pressure volumetric study. *J. Phys. Chem. C* **111**, 16131–16137 (2007).

4. Mardirossian, N. & Head-Gordon, M. ωB97M-V: A combinatorially optimized, range-separated hybrid, meta-GGA density functional with VV10 nonlocal correlation. *J. Chem. Phys.* **144**, 214110 (2016).

5. Vydrov, O. A. & Van Voorhis, T. Nonlocal van der Waals density functional: The simpler the better. *J. Chem. Phys.* **133**, (2010).

6. Hurley, M. M., Pacios, L. F., Christiansen, P. A. Ross, R. B. & Ermler, W. C. Ab initio relativistic effective potentials with spin-orbit operators. II. K through Kr. *J. Chem. Phys.* **84**, 6840–6853 (1986).

7. Whittleton, S. R., Boyd, R. J. & Grindley, T. B. Evaluation of effective core potentials and basis sets for the prediction of the geometries of alkyltin halides. *J. Phys. Chem. A* **110**, 5893–5896 (2006).

8. Christiansen, P. A., Lee, Y. S. & Pitzer, K. S. Improved ab initio effective core potentials for molecular calculations. *J. Chem. Phys.* **71**, 4445–4450 (1979).

9. Christiansen, P. A., Balasubramanian, K. & Pitzer, K. S. Relativistic ab initio molecular structure calculations including configuration interaction with

application to six states of TlH. *J. Chem. Phys.* **76**, 5087–5092 (1982).

10. Pitzer, K. S. Relativistic calculations of dissociation energies and related properties. *Int. J. Quantum Chem.* **25**, 131–148 (1984).

11. Pitzer, K. S. Electron structure of molecules with very heavy atoms using effective core potentials. *Relativistic Effects in Atoms, Molecules, and Solids* 403–420 (Springer US, 1983).

12. Christiansen, P. A. & Pitzer, K. S. Improved ab initio effective potentials for Ar, Kr, and Xe with applications to their homonuclear dimers. *J. Chem. Phys.* **75**, 5410–5415 (1981).

13. Shao, Y. *et al.* Advances in molecular quantum chemistry contained in the Q-Chem 4 program package. *Mol. Phys.* **113**, 184–215 (2015).

14. Baker, J., Kessi, A. & Delley, B. The generation and use of delocalized internal coordinates in geometry optimization. *J. Chem. Phys.* **105**, 192–212 (1996).

15. Baker, J. An algorithm for the location of transition states. *J. Comput. Chem.* **7**, 385–395 (1986).

16. Weigend, F. & Ahlrichs, R. Balanced basis sets of split valence, triple zeta valence and quadruple zeta valence quality for H to Rn: Design and assessment of accuracy. *Phys. Chem. Chem. Phys.* **7**, 3297–3305 (2005).

17. Horn, P. R., Mao, Y. & Head-Gordon, M. Probing non-covalent interactions with a second generation energy decomposition analysis using absolutely localized molecular orbitals. *Phys. Chem. Chem. Phys.* **18**, 23067–23079 (2016).

18. Horn, P. R., Mao, Y. & Head-Gordon, M. Defining the contributions of permanent electrostatics, Pauli repulsion, and dispersion in density functional theory calculations of intermolecular interaction energies. *J. Chem. Phys.* **144**, 114107 (2016).

19. Levine, D. S., Horn, P. R., Mao, Y. & Head-Gordon, M. Variational energy decomposition analysis of chemical bonding. 1. Spin-pure analysis of single bonds. *J. Chem. Theory Comput.* **12**, 4812–4820 (2016).

20. Xantheas, S. S. On the importance of the fragment relaxation energy terms in the estimation of the basis set superposition error correction to the intermolecular interaction energy. *J. Chem. Phys.* **104**, 8821–8824 (1996).

21. Simon, S., Duran, M. & Dannenberg, J. J. How does basis set superposition error change the potential surfaces for hydrogen-bonded dimers? *J. Chem. Phys.* **105**,

11024–11031 (1996).

22. Sordo, J. A., Chin, S. & Sordo, T. L. On the counterpoise correction for the basis set superposition error in large systems. *Theor. Chim. Acta* **74**, 101–110 (1988).

23. Baker, J. Constrained optimization in delocalized internal coordinates. *J. Comput. Chem.* **18**, 1079–1095 (1997).